Orbital control of relative sea-level changes in the Plio-Pleistocene of the north-western Brazilian Equatorial Margin

Lucas Tortarolo[a,b,g,h], Marina Rabineau[a], Slah Boulila[b,c], Christian Gorini[b], Damien Do Couto[b], Antonio Tadeu Dos Reis[d], André W. Droxler[e], Alberto Machado Cruz[f], Cleverson Guizan Silva[g]

[a] Laboratoire Geo-Ocean, Institut Universitaire Européen de la Mer, UBO, UBS, IFREMER, CNRS, UMR6538, Rue Dumont d'Urville, 29280 Plouzané, France

[b] Sorbonne Université, CNRS, Institut des Sciences de la Terre Paris, Paris F-75005, France.

[c] Astronomie et Systèmes Dynamiques/Institut de Mécanique Céleste et de Calcul des Ephémérides, CNRS-UMR8028, Observatoire de Paris, Paris Sciences & Lettres University, Sorbonne Université, Paris 75014, France.

[d] Departamento de Oceanografia Geologica, Universidade do Estado do Rio de Janeiro, Rua São Franscisco Xavier, 524, Rio de Janeiro, RJ, Brazil

[e] Department of Earth, Environmental and Planetary Sciences, Rice University, 6100 Main St., Houston, TX 77005, USA

[f] Beicip-Franlab, Rua da Assembléia, 10 - Centro, Rio de Janeiro - RJ, 20011-901, Brazil

[g] Departamento de Geologia e Geofísica, Universidade Federal Fluminense, Av. Gal. Milton Tavares de Souza, Campus da Praia Vermelha, Boa Viagem, Niterói, RJ, Brazil

[h] Eliis, 3 Rue Jean Monnet, 34830 Clapiers, France

corresponding author: lucas.toratorolo@eliis.fr

Abstract

The Brazilian Equatorial Margin is strongly influenced by sediment supply from the Amazon River, where the Plio-Pleistocene succession lacks geochronological data making the stratigraphic architecture of this continental margin and its driving mechanisms poorly understood. Here we study a shelf-edge area of the Brazilian Equatorial Margin when siliciclastic deposition started around 3.7 to 4 Ma immediately after the well-known Amapá carbonate platform. We perform a coupled approach of sequence stratigraphic analysis of a 3D seismic block, and cyclostratigraphic analysis of gamma-ray (GR) log data from three exploration wells. We identify nine main seismic sequences since the onset of siliciclastic deposition. Cyclostratigraphic analyses indicate that each seismic sequence corresponds to a long 405 kyr eccentricity cycle. Additionally, we show that the nine 405 kyr eccentricity related seismic sequences are grouped into three depositional mega-sequences (MS-I through MS-III), which mark major changes in stratal architecture along the Brazilian Equatorial shelf edge. Orbitally calibrated mega-sequence boundaries yield ages of 3.7, 2.4 and 0.8 Ma for the bases of MS-I, MS-II and MS-III respectively. Correlation of these mega-sequence boundaries with the global sea-level change suggests that long-term increase in the amplitude of sea-level

fluctuations is likely the primary driver of these major sedimentary changes. We suggest that basal mega-sequence boundaries of MS-II and MS-III at 2.4 and 0.8 Ma may reflect important steps in the Earth's Quaternary climate and sea level, specifically overall cooling that led to the intensification of Northern Hemisphere Glaciations (iNHG) and the Mid-Pleistocene Transition (MPT). Finally, a further significant change in shelf edge architecture at around 0.4 Ma corresponds to a change from mostly prograding patterns since 0.8 Ma to mostly aggrading ones during the last 405 kyr. This shift in the depositional system is likely related to the prominent high amplitude sea-level rise characterizing the long-lasting Marine Isotopic Stage 11.

Keywords: Brazilian Equatorial Margin, Offshore Amazon Basin, Plio-Pleistocene, cyclostratigraphy, seismic and sequence stratigraphy, astro-climate.

1. Introduction

The Amazon River plays a significant role in Earth's hydrologic budget, contributing to 20% of global fluvial input to the oceans (Dai and Trenberth, 2002). Covering 35.5% of the South American continental surface, the Amazonian hydrographic basin is the world's largest drainage basin (Milliman, 2001; Nittrouer et al., 1986), and contains the Amazonian Forest and ecosystem, which serve as vital indicators of Earth's climate (Malhi et al., 2008). The Amazon River acts as a biological barrier on land and in sea due to its prominent sediment plume and high concentrations of suspended material and nutrients that spreads for thousands of kilometres over the North Brazilian Continental Shelf and adjacent open waters (Giachini Tosetto et al., 2022). As a result, the impact of climate on the supply of water and sediment along the Amazon River, recorded in the stratigraphic succession of the adjacent continental margin, has received increasing attention in recent years, from a broad scientific community including geoscientists, oceanographers, and biologists.

The stratigraphic succession of the Amazon continental margin documents intricate forcing processes from climate, precipitation and sea level which drive sediment supply over time. A seminal study based on 2D seismic and well-log analysis showed the dominance of sea-level variations in shaping the Amazon offshore sedimentary system (Damuth and Kumar, 1975). During sea level highstands, sedimentary deposits primarily accumulate nearshore, while suspended sediments are transported by longshore currents, partially accumulating along the northern Brazilian coastline or reaching the French Guiana shelf and beyond (Eisma and van der Marel, 1971; Jacobs and Ewing, 1969; Milliman et al., 1975). When sea level decreases and reaches the shelf edge, terrigenous sediments from the Amazon are intercepted by the Amazon Canyon, bypassing the outer shelf and accumulating directly on the well-developed Amazon deep-sea fan along the Brazilian margin's slope (Damuth et al., 1983; Damuth and Kumar, 1975).

Gaining a deeper comprehension of the impact of sea level fluctuations and the broader influence of climate has been the central theme of numerous studies (Behling et al., 2000; Crivellari et al., 2018; Hoorn, 1997; Nace et al., 2014; Rühlemann et al., 2001; Zhang et al., 2015). However, these studies are focused on the last glacial-interglacial cycles, spanning up to a maximum of 400,000 years.

Earth's orbital parameters exert a strong effect on global climate and sea level, particularly Earth's orbital eccentricity dominated the global climate during the last million years, and may impact the Amazon drainage basin and margin as well (Gorini et al., 2014). Nevertheless, our understanding of the impact of climate change on sediment accumulation over longer time spans remains less clear due to limited data availability and quality near the Amazon River mouth. Although more than 40 exploration wells have been drilled on the Amazon shelf, they typically target deeper sedimentary formations and contain limited information on the Plio-Quaternary succession. Biostratigraphic data for the Plio-Pleistocene succession are scarce, resulting in a poorly constrained age model, which impacts our comprehension of the evolution through time of the Amazon continental margin architecture.

This study examines for the first time a detailed Plio-Pleistocene stratigraphy of the Amazon margin, using a 3D seismic block and well-log data from three nearby boreholes. We use an integrated approach of cyclostratigraphy based on gamma-ray logs, and sequence stratigraphy based on the analysis of 3D seismic block. Using this integrated approach, we aim to decipher the main sediment sequences and packages of the Amazon shelf edge, and to unreveal the main driving mechanisms of its evolution over time.

2. Geological setting

The Brazilian Equatorial Margin (*Figure 1*) was formed in two steps during the opening of the Equatorial Atlantic Ocean: an early step during the Late Triassic Epoch through the Jurassic Period (~225-145 Ma) leading to the opening of the Central Atlantic Ocean, and a later step associated with continental rifting during the Early Cretaceous (~120–105 Ma) (Darros de Matos, 2000). Open-marine deposition began around the Albian with the clastics Limoeiro Formation (approximately 102 Ma) and persisted until the Palaeocene Figueiredo et al. (2007). From the late Palaeocene (around 59 Ma) to the late Miocene, the basin was dominated by mixed carbonate-siliciclastic shelf sediments (Marajo and Amapá Formations) (Figueiredo et al., 2007). From the late Miocene onward, increasing clastic sediment influx led to the burial of the carbonate platform (Gorini et al., 2014), resulting in the formation of the present-day Offshore Amazon Basin including continental shelf deposition and the Amazon Fan laying on the slope and abyssal plain. The events triggering the transition from carbonates to silico-clastic sedimentation remain a subject of ongoing debate (Campbell, 2010; Cruz et al., 2019; Figueiredo et al., 2010, 2009; Gorini et al., 2014).

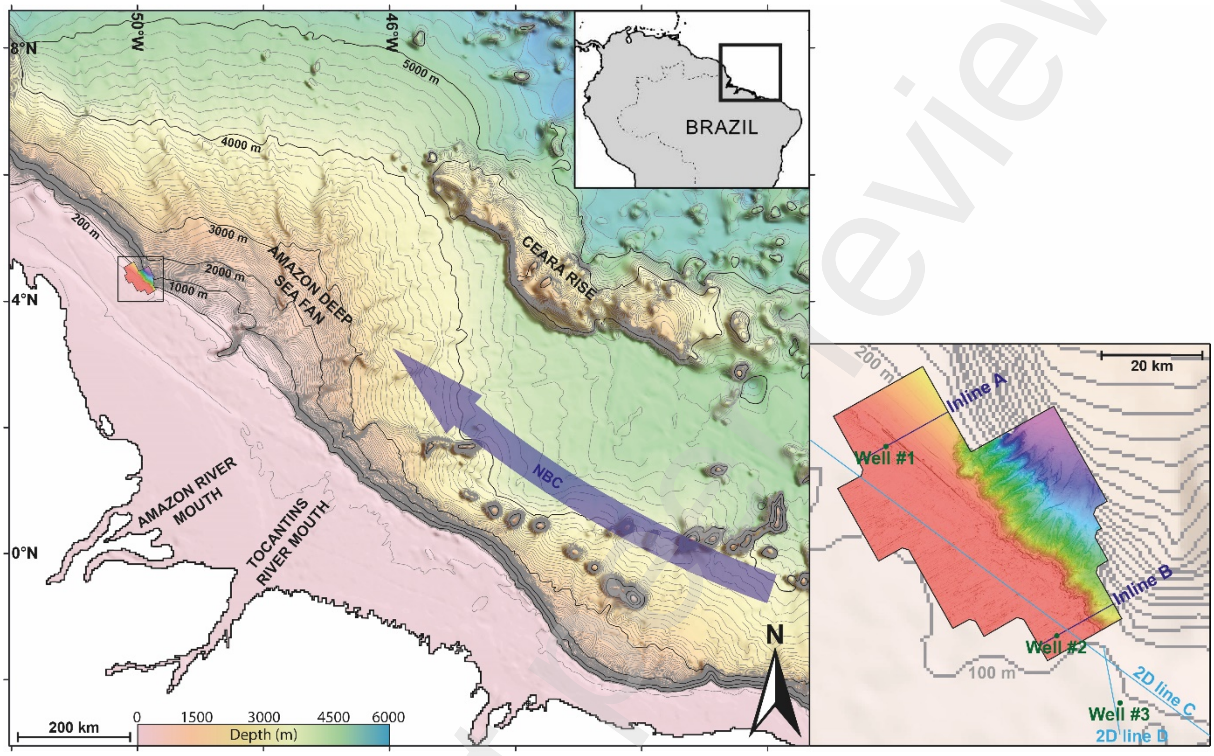

Figure 1: Bathymetric map of the NW Equatorial Brazilian Margin along with the location of sites of the studied data. The 3D seismic block is shown with the sea floor topography. The North Brazilian Current (NBC) is indicated with a thick blue arrow (Note the current also sweeps the continental shelf, the arrow is only indicative). In the expanded view, three wells are displayed in green (well #1 and #2 inside the 3D block, and well #3 outside the 3D block); two inlines A and B in dark blue are interpreted in figures 4 and 5, in addition to two 2D seismic lines C and D (also shown) used to tie the well #3 with the 3D seismic block.

Various studies of the stratal architecture of the Offshore Amazon Basin have proposed a Late Miocene age for the cessation of carbonate sedimentation, marked by the top of the Amapá Formation, linked to an increase in siliciclastic sediments due to the initiation of the transcontinental Amazon River (Brandao and Feijo, 1994; Campbell, 2010; Carozzi, 1981; Figueiredo et al., 2010, 2009; Silva et al., 1998; Wolff and Carozzi, 1984). However, recent research suggests that carbonate sedimentation persisted in the Offshore Amazon Basin well after the Late Miocene (Cruz et al., 2019; Gorini et al., 2014). In particular, Cruz et al. (2019) used calcareous nannofossil zonations in well data to re-evaluate the study of Figueiredo et al. (2009), taking into account the variability in the cessation of carbonate deposition proposed by

Gorini et al. (2014). This led to the establishment of a Late Miocene age (8 million years) for the cessation of carbonate sedimentation in the southern part of the Brazilian Equatorial shelf, versus an Early Pliocene age (3.7-4.1 Myrs, *Figure 2*) in the northern sector of the basin (near Well #3).

The Offshore Amazon Basin lies in the northwestern portion of the Brazilian Equatorial Margin (*Figure 1*) and encompasses an area of approximately 360,000 km² (Silva et al., 1998). The basin corresponds to a depocenter in front of the Amazon River Mouth, containing up to 9 km of siliciclastic sediments. Between 8 to 3.7 million years, most of the clastic sediments were trapped in a paleo-embayment in front of the Amazon River mouth (Cruz et al., 2019). Following the embayment's completion, sediment progradation commenced, primarily toward the northeast due to the influence of the North Brazilian Current (NBC), which continues to impact the Amazon plume and facilitate sediment migration toward the northern part of the margin (Gensac et al., 2016; Hu et al., 2004). During periods of falling sea levels, the slope and basin experience significant influence from Amazon-derived sediments deposited into the Amazon deep-sea fan via the Amazon Canyon (Flood et al., 1995; Maslin et al., 2006). In proximity to the canyon, the deep-sea fan expands to around 380 km in width and extends to the abyssal plain at depths reaching approximately 4850 m (Damuth and Kumar, 1975). The thickness of sediment within the Amazon fan (reaching up to 9 km) has prompted isostatic subsidence and lithospheric flexural deformation beneath the fan and surrounding regions, including the outer shelf (Cruz, 2018; N. W. Driscoll and Karner, 1994; Rodger et al., 2006; Silva et al., 1998).

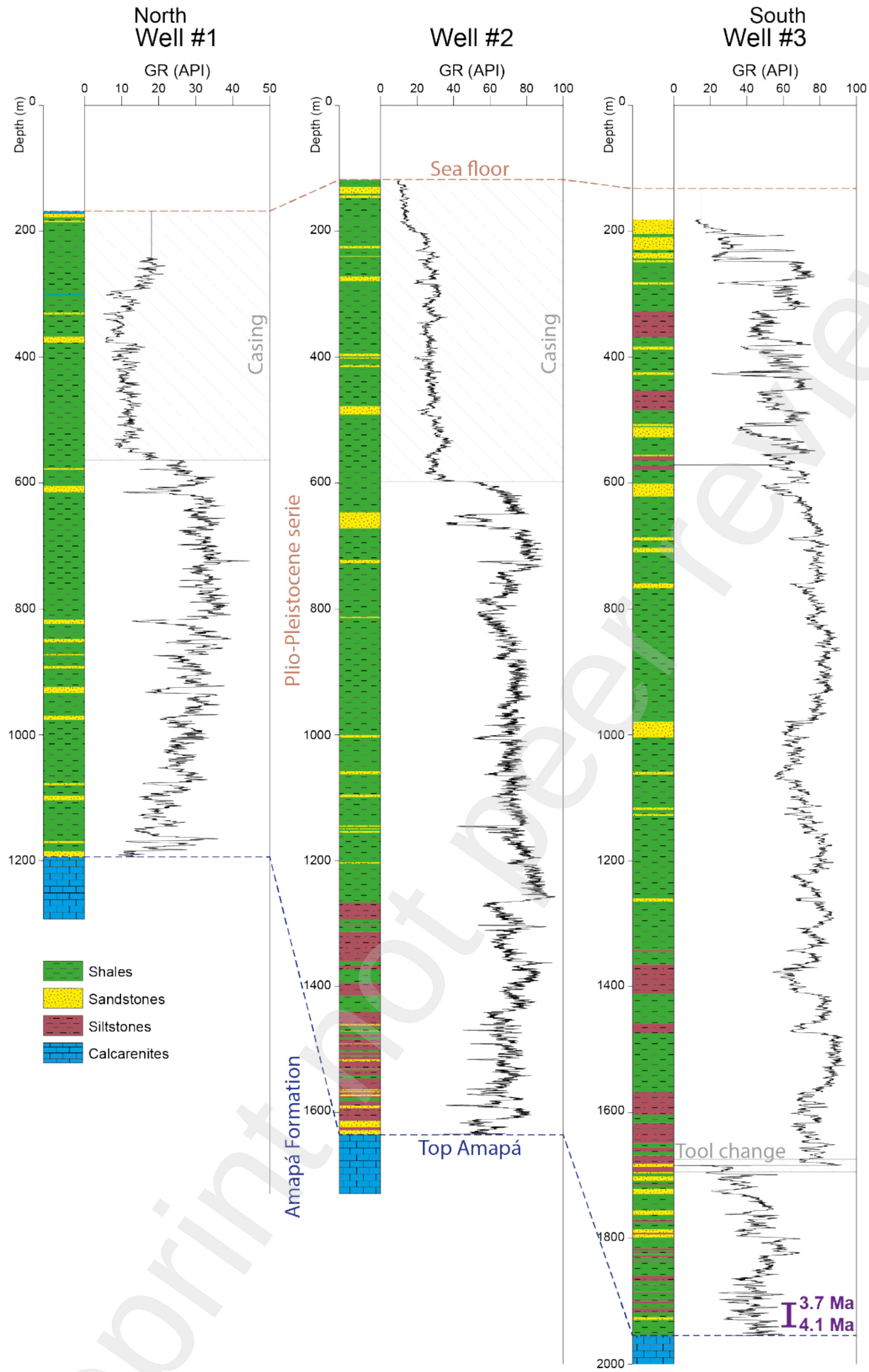

Figure 2: Lithology and gamma ray (GR) data of Wells #1, #2 and #3 (Plio-Pleistocene interval) shown from left north (Well #1) to right south (Well #3). The purple interval at the beginning of the Plio-Pleistocene section, just above the top Amapá Formation, in Well #3 was dated by biostratigraphy at 3.7 to 4.1 Ma (Cruz et al., 2019). Some unusual changes in the GR values, due to technical issues such as the presence of casing or tool change, are noted in light grey along the wells.

3. Data and methods

3.1. 3D seismic and downhole datasets

This study uses a 3D seismic block up to 60 km long and 40 km wide, with a grid spacing of 25 meters, encompassing 2387 inlines and 1733 crosslines (*Figure 1*). The seismic volume was processed using a standard sequence that included pre-stack time migration (PSTM). The data has a vertical sampling interval of 4 ms, and the full-stack signal exhibits a dominant frequency of 37 Hz, offering a vertical resolution of 10-20 m for velocities from 1500 to 3000 m/s.

Downhole data were used from three wells situated within or near the 3D seismic block (*Figure 1*), which span the entire Plio-Pleistocene series (*Figure 2*). These three wells labelled APS44, APS29, and APS45B, are referred henceforth to Wells #1, #2, and #3, respectively. Wells #1 and #2 are situated within the 3D seismic block, while Well #3 is 17 km southeastern of the 3D seismic block (*Figure 1*). Gamma-ray (GR) log data have a depth resolution of 15-20 cm. GR values are expressed in API (American Petroleum Institute) unit. GR data are available from seafloor in Well #2, and below depths 75 m and 49 m in Wells #1 and #3, respectively. Significant shifts in GR values around 560 m in Well #1 and 600 m in Well #2 are associated with the presence of casings in the upper intervals rather than lithological variations. A rough lithological description based on a low-resolution (3 to 5 m) mud sampling are available for the three wells (*Figure 2*). The biostratigraphic age model is poorly constrained. Only two potential calcareous nannofossil age ranges in Well #3 were defined (Cruz et al., 2019). The first age ranges from 3.7 to 3.92 Ma, which is inferred from the recognition of the Last Occurrence (LO) of *Sphenolithus Neoabies* at depth 1910 m. The second age ranges from 3.92 to 4.13 Ma, which is based on the detection of the First Occurrence (FO) of *Discoaster tamalis* at depth 1940 m. These biostratigraphic data are projected onto Wells #1 and #2, and correlated from the wells to the 3D seismic dataset (*Figure S1*).

3.2. Seismic sequence stratigraphic methods

A standard seismic analysis approach (Mitchum and Vail, 1977) was used for the 3D seismic data based on the recognition of reflection termination such as onlap, erosional truncations, seismic facies/configuration and vertical stacking patterns. This method led to the creation of a seismic facies and architectural element catalogue (*Figure 3*).

Seismic data	Seismic interpretation	Description	Interpretation
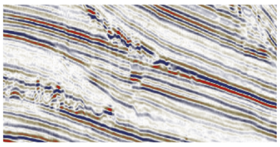	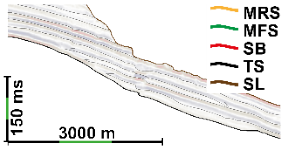	SF1: Mostly aggrading, continuous, sub-parrallels, medium amplitude reflectors with onlap	SF1: Transgressive System Tract (TST)
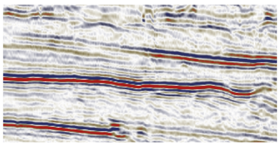	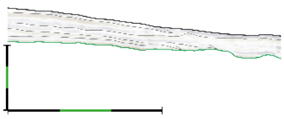	SF2: Prograding and aggrading continuous, convergent, medium amplitude reflectors with downlap	SF2: Highstand System Tract (HST)
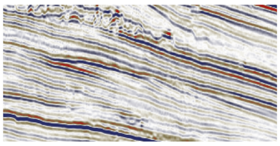	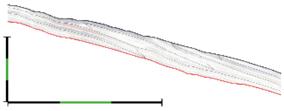	SF3: Only prograding, continuous, low amplitude reflectors with offlap and downlap	SF3: Falling Stage System Tract (FSST) along the outer shelf
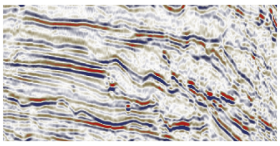	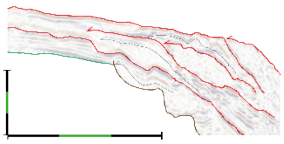	SF4: Mostly prograding, continuous, medium to low amplitude reflectors with high inclination, offlap and downlap	SF4: Falling Stage System Tract (FSST) and/or Lowstand System Tract (LST: if there is aggrading pattern) located on the slope
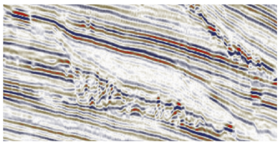	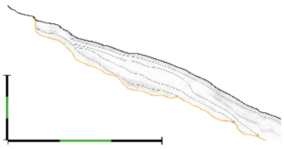	SF5: Mostly prograding and slightly aggrading, low amplitude reflectors with onlap and downlap	SF5: Lowstand System Tract (LST) located on the slope
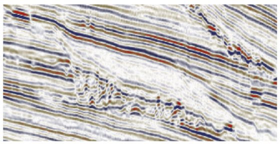	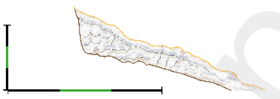	SF6: Chaotic, discontinuous, medium amplitude reflectors	SF6: Submarine Landslide (SL)
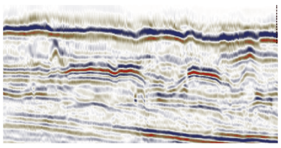	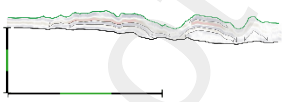	SF7: High amplitude reflectors with build-up geometries	SF7: Transgressive carbonates

Figure 3: Seismic facies classification and interpretation of stratigraphic elements and geometries.

In addition to the seismic analysis, a sequence stratigraphy model has been developed (*Figure 4*). Each of the observed facies is interpreted in terms of system tracts, following the stratigraphic sequence definition put forth by Catuneanu (2019, 2006) and Catuneanu et al. (2011, 2009). According to this definition, a stratigraphic sequence consists of a succession of strata deposited during a complete cycle of change in accommodation space or sediment supply. Accommodation, representing the relative volume available for sediments at a given time, is primarily influenced by two mechanisms: eustatic fluctuations and subsidence (Catuneanu et al., 2011). This definition is particularly evident in the shelf to upper slope areas with relatively shallow environments. In deeper settings, such as the lower slope and deep basin, the effects of hydrodynamics and currents must be considered more carefully, as they could generate significant deposits such as turbidites or contourites.

Consequently, a sequence is composed of various system tracts, each corresponding to different stages in the variation of the ratio between accommodation rate and sediment supply (A/S ratio). We used the Depositional Sequence IV, introduced by Hunt and Tucker (1992) and Helland-Hansen and Gjelberg (1994) to define each system tract. According to this model, a complete sequence cycle comprises four distinct system tracts: The Transgressive System Tract (TST), The Highstand System Tract (HST), The Falling Stage System Tract (FSST), and the Lowstand System Tract (LST).

Moreover, since progradation typically takes place as a continuous depositional process from Highstand to Lowstand conditions, identifying and correlating the Sequence Boundaries (SBs), limiting the FSST to the LST, on a regional scale can be challenging. As a result, we prefer to use the reflectors corresponding to the Transgressive Surface (TS) as markers for sequence boundaries.

In pursuit of a comprehensive understanding of the study area's evolution, the interpretation and analysis of stratigraphic sequences were conducted using specialized 3D seismic interpretation software, PALEOSCAN (https://www.eliis-geo.com).

3.3. Cyclostratigraphic methods and time-series analysis

We use gamma-ray (GR) data as an indirect paleoclimatic proxy for characterizing orbitally-driven continental and marine sediments (e.g., Ruffell and Worden, 1999; Weedon et al., 2004; Wu et al., 2013). Since the Gamma-Ray (GR) data does not start at the seafloor in Wells #1 and #3, we extended the signal to cover this depth. Afterward, we detrend the GR dataset using the weighted-average lowess method (Cleveland, 1979) to mitigate abrupt changes resulting from acquisition issues like tool changes and cased intervals as well as to eliminate linear and parabolic trends that could reduce the amplitude of higher frequency cycles. Subsequently, we use the multi-taper method (MTM) spectral analysis to seek for sedimentary cyclicities within GR data (Thomson, 1982). The manual frequency ratio method, such as the 5:2:1 relationship among short eccentricity (~100 kyr), the obliquity component (~41 kyr), and precession (~20 kyr), aids in identifying potential astronomical cyclicities. We use a Gaussian filter to extract target astronomical cycles (Paillard et al., 1996). We filter to the short eccentricity band, which is the most prominent astronomical cycle in GR datasets. We then construct age model for Wells #1 and #3 by aligning the minima of the filters with minima of Earth’s short eccentricity from the La2004 astronomical solution (Laskar et al., 2004). Well #2 crosses the lower siliciclastic series, a highly deformed area, therefore the GR dataset of Well #2 is not suitable to build an age model for the whole siliciclastic series and only the upper interval is studied in this paper (*Figure S2*). To obtain a geochronological anchor point at the top of studied wells, we used the radiocarbon dating conducted on samples collected at the seafloor within the seismic block by Vale et al. (2022), which are dated to approximately 15,000 years BP. These samples consist of carbonate rocks and are equivalent to the lithological description at the seafloor along Well #1 (*Figure 2*). Lastly, we compare our age model with the outcomes of the "eCOCO" method. The "eCOCO" tool is based on the COrrelation COefficient method (Li et al., 2019) and allow to study sedimentation rate evolution across datasets. The COCO technique, inspired by the average spectral misfit (ASM) method of Meyers and Sageman (2007), is an automatic frequency ratio method. It estimates the correlation coefficient between the power spectra of an astronomical target signal and paleoclimate proxy series across a range of tested sedimentation rates. Similar to ASM, a null hypothesis of no astronomical forcing is assessed through Monte Carlo simulation prior to validating our results. The analysis steps were performed using Acycle v2.0 software (Li et al., 2019).

4. Results

4.1. Dating the onset of the siliciclastic deposition

A prominent and continuous high-amplitude reflector (*Figure 4*) marks the top of the Amapá Formation. In the wells, this reflector corresponds to a lithological change from sand-sized carbonates to fine-grained siliciclastic sediments, and covers nearly the entire surface of the seismic block. A second thick, continuous, high-amplitude reflector represents the seafloor, defining the top of the Plio-Pleistocene series.

Only one biostratigraphic age point in Well #3 spanning 3.7-4.1 Ma is available at the base of the siliciclastic Formation (*Figure 2,* see Data and Methods). Well #3 is just outside the 3D seismic block. We thus followed the position of the biostratigraphic point from Well #3 along 2D seismic lines crossing Well #3 towards our 3D seismic block (see *Figure S1*). The correlation falls just above the Amapá carbonate platform and in the first reflections of the siliciclatic sediment in Well #2 (*Figure S1*). Therefore, we suggest an age of around 4 Ma for the onset of post Amapá siliciclastic sediments in our studied area.

4.2. Stratigraphic sequences

4.2.1. Seismic facies and associated sedimentary architecture

We identified seven seismic facies (SF1 through SF7, *Figure 3*) based on a detailed analysis of the geometry, terminations, and impedance of seismic reflectors, and provided an interpretation in terms of depositional architecture.

- SF1 consists of stacked horizontal and parallel reflectors with high amplitude and good lateral continuity (corresponding to a high impedance contrast between beds). SF1 overlaps other seismic facies, displaying onlapping terminations. SF1 is capped by a distinct prograding clinoform surface (base of the HST), therefore it corresponds to a Transgressive System Tract (TST).

- SF2 comprises seismic reflectors of medium amplitude and low lateral continuity, with mostly sub-horizontal and sub-parallel reflectors. Sigmoidal to oblique reflections corresponding to basinward prograding foresets allow clear differentiation of this seismic unit from the TST. This seismic facies is linked to a Highstand System Tract (HST).

- SF3 is characterized by clinoforms (oblique) towards the basin of low to medium amplitude reflectors with steep angles. Reflectors are toplapping and outward building into the basin, exhibiting downlaps at the base of the seismic unit. This facies displays progradation only with a clear downward shift of toplaps that links it to the Falling Stage System Tract (FSST).

- SF4 is defined by inclined reflectors of medium to low amplitude with steep angles, and is topped by one or two high-amplitude reflectors. Reflectors show progradation, while a minor aggradational component is visible in some parts. This seismic facies is hence linked to a Falling Stage System Tract (FSST) or/and a Lowstand System Tract (LST) on the slope, contingent on the presence or absence of aggradation.

- SF5 is marked by very low amplitude reflectors that prograde and aggrade. This facies exhibits onlap and downlap terminations and is associated with the Lowstand System Tract (LST) or early Transgressive System Tract (TST).

- SF6 features discontinuous and deformed reflectors of medium to high amplitude. Due to its internal geometry and position along Submarine Landslide scar (SLi), it is linked to mass transport deposits.

- SF7 is characterized by high amplitude and low-frequency reflectors, sometimes presenting a lateral shift in polarity. This seismic facies is also associated with topographic high features. The combination of these characteristics suggests the occurrence of carbonate build-ups.

4.2.2. Lithologies and general settings

The Pliocene-Pleistocene series of the studied wells is primarily composed of shales, accounting for approximately 90% of the drilled lithologies, with sandstone being the second most abundant lithology (*Figure 2*). Some siltstones are also observed in the lower part of the series, closer to the Amazon River mouth (Wells #2 and #3; *Figure 2*). Finally, calcarenites constitute around 1% of the recovered sediments.

The thickness of the Plio-Pleistocene series varies in function of the distance from the Amazon River mouth. It is thicker in the southern part of the seismic block, reaching 1822 m at Well #3, and 1514 m at Well #2, while it significantly decreases to 1026 m at Well #1 in the northern part of the seismic block. The primary morphology of the Plio-Pleistocene series features slightly tilted reflectors prograding towards the North-East (*Figure 4*).

4.2.3. Seismic sequences and their organization into mega-sequences

Stratigraphic interpretation of the 3D seismic data allowed the identification of nine seismic sequences (S1 through S9, *Figure 4*) defined as a succession of strata deposited during a complete cycle of change in accommodation space (A) or sediment supply (S) and identified by the succession of various system tracts, each corresponding to different stages in the variation of the ratio between accommodation rate and sediment supply (A/S ratio). The TS is used as sequence boundary and is defined by the change from mostly prograding to mostly aggrading condition. The surface is characterized by extensive retrogradational stacking patterns showing numerous onlap terminations. Based on common characteristics, the nine seismic sequences were grouped into three distinct mega-sequences, referred to as MS-I, MS-II, and MS-III and decribed as follows.

MS-I includes seismic sequences S1, S2, and S3 which is 374 m thick in Well #1 and encompasses the lower part of the Plio-Pleistocene series (*Figure 4*). Transgressive System Tracts (TSTs) are not clearly identified within S1 to S3, as the onlap terminations that typically define these seismic sequences are not discernible in this mega-sequence. Nevertheless, there are thick high-impedance reflectors covering the top of the underlying regressive pattern. Sometimes, these reflectors appear notably thicker toward the continent with apparent onlap, and were thus identified as TSTs, with the higher impedance contrast may be linked to sand deposits (*Figure 2*, Well #1). Highstand System Tracts (HSTs) and Falling Stage System Tracts (FSSTs) within S1 to S3 exhibit reflectors with low steepness. Furthermore, the foresets of the clinoforms within S1 to S3 are well-developed and can extend over tens of kilometers in length. Erosion within S1 to S3 remains limited (*Figure 4*). Notably, the thicknesses of S1 to S3 exhibit a clear decrease over time in Well #1 (*Figure 4*) due to important progradation.

MS-II comprises seismic sequences S4 through S7, which is 388 m thick in Well #1 (*Figure 4*). Seismic sequences S4 through S7 share common features, including increasing TST thicknesses compared to sequences S1 through S3 that compose MS-I. In MS-II, the TSTs are characterized by stacked sub-parallel reflectors with onlapping terminations, displaying a thick aggrading pattern. Internal reflectors within clinoforms show a notable increase in steepness and a reduction in bottomset extension relative to MS-I. The most significant change among MS-I and MS-II is extensive erosion observed in MS-II (*Figure 4*). S4 to S7 are significantly affected by erosion, either on the outer shelf or on the slope. Submarine landslides along the slope have removed substantial sediment volumes, while on the outer shelf, the Transgressive Surface (TS) is marked by erosive unconformities.

MS-III comprises seismic sequences S8 through S9 and is only 264 m thick in Well #1 (*Figure 4*). MS-III is distinguished by a shift of sediment accumulation into the slope area, leading to a substantial increase in progradation rates. On the slope, sub-seismic cycles are evident, corresponding to nine smaller-scale Falling Stage System Tracts (FSSTs) (referred to as FR1 to FR9 in *Figure 4*). These sub-cycles are only observed within S8 and S9. Consequently, S8 and S9 have been classified under a separate mega-sequence. Their morphologies and distribution differ from the seven main FSSTs observed in MS-I and MS-II. The nine FSSTs FR1-FR9 can be categorized into two groups. The first five regressions (FR1 to FR5) only exhibit progradations with a shift toward the basin (*Figure 4*). Conversely, the four younger regressions (FR6 to FR9), situated at the top of the Plio-Pleistocene series, display a distinct high aggradation pattern. Their geometries vary from the south to the north, featuring very steep reflectors along Inline B (*Figure 4*) and low-angle reflectors along Inline A (*Figure 4*). MS-III is also distinctive for the emergence and development of steep canyons along the slope and the abundance of carbonate build-ups (SF7; *Figure 3*).

Extensive descriptions of the above seismic mega-sequences are available in the supplementary material.

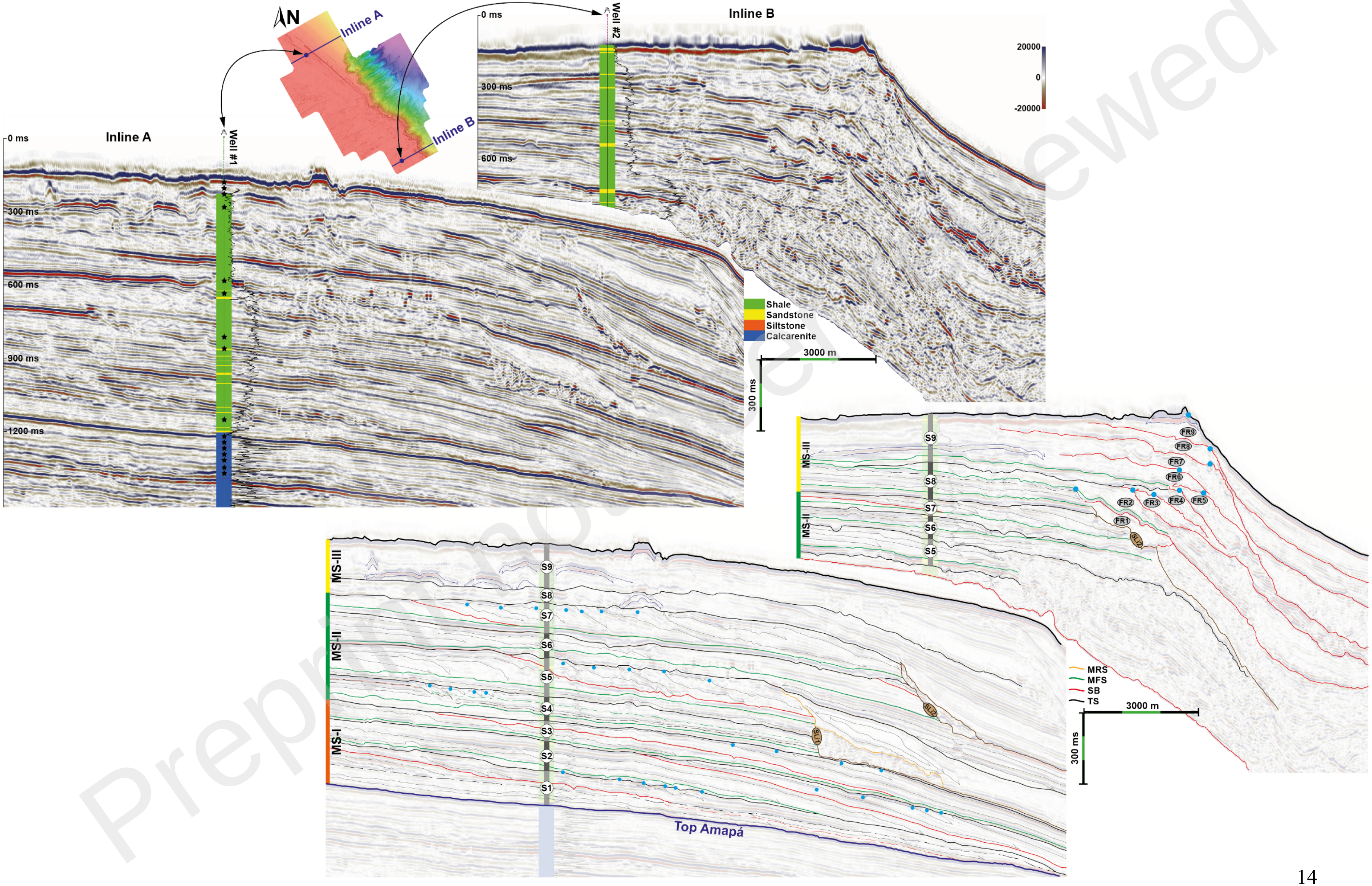
N
Inline A
Inline B
0 ms
300 ms
600 ms
900 ms
1200 ms
Well #1
Well #2
20000
0
-20000
Shale
Sandstone
Siltstone
Calcarenite
3000 m
300 ms
MS-III
MS-II
MS-I
S9
S8
S7
S6
S5
S4
S3
S2
S1
FR1
FR2
FR3
FR4
FR5
FR6
FR7
FR8
FR9
SL1
SL2
Top Amapá
MRS
MFS
SB
TS

Figure 4: Inlines A and B crossing respectively Wells #1 and #2 (See location in Figure 1). Lithology and GR data are shown along the wells. Black stars in Well #1 log show the check shots position used for the time-depth conversion. The three intervals in orange, green, and yellow at the left side of the lower profiles, depicts the three interpreted mega-sequences (labelled MS-I though MS-III). In the interpreted profiles, along the wells, grey-shaded intervals noted S1 through S9 indicate the nine identified seismic sequences. Brown lines in the lower profiles (labelled SLi1 and SLi2) emphasize two Submarine Landslides scars and deposits. Light blue dots highlight potential shoreline position during lowest sea level. In the interpreted Inline B, labels FR1 through FR9 depict the identified regressive prisms (Forced Regression 1 through 9) inside the last two seismic sequences.

4.3. Cyclostratigraphy

The Multi-Taper Method (MTM) spectral analysis of the Gamma-Ray (GR) datasets in depth domain reveals numerous frequencies (*Figure 5*). Using manual frequency ratio method, we identified three frequency bands in each well matching frequency ratios of short eccentricity (97-128 kyr), obliquity (41 kyr), and precession (19-23 kyr). In Well #1, short eccentricity wavelengths range from 25 to 35 m, obliquity wavelength is about 11 m, and precession wavelength is about 6 m. In Well #2, 32 m wavelength is interpreted as short eccentricity, 12 m wavelength as obliquity, and 6 m wavelength as precession (*Figure S2*). Finally, in Well #3, 46 m wavelength corresponds to short eccentricity, 21 m to obliquity, and 11 m to precession (*Figure 6*). The increase in cycle wavelength from north to south, i.e. from Well #1 to Well #3, reflects an increase in sedimentation rate due to decreasing distance to the mouth of the Amazon River. Additionally, there is a longer wavelength of 172 m in Well #3, which may correspond to the 405 kyr long eccentricity (Figures 6 and S2). Broad bandpass filters have been applied to the potential Earth's short eccentricity for each well (*Figures 5 and 6*) to orbitally tune the GR data (Figure 7).

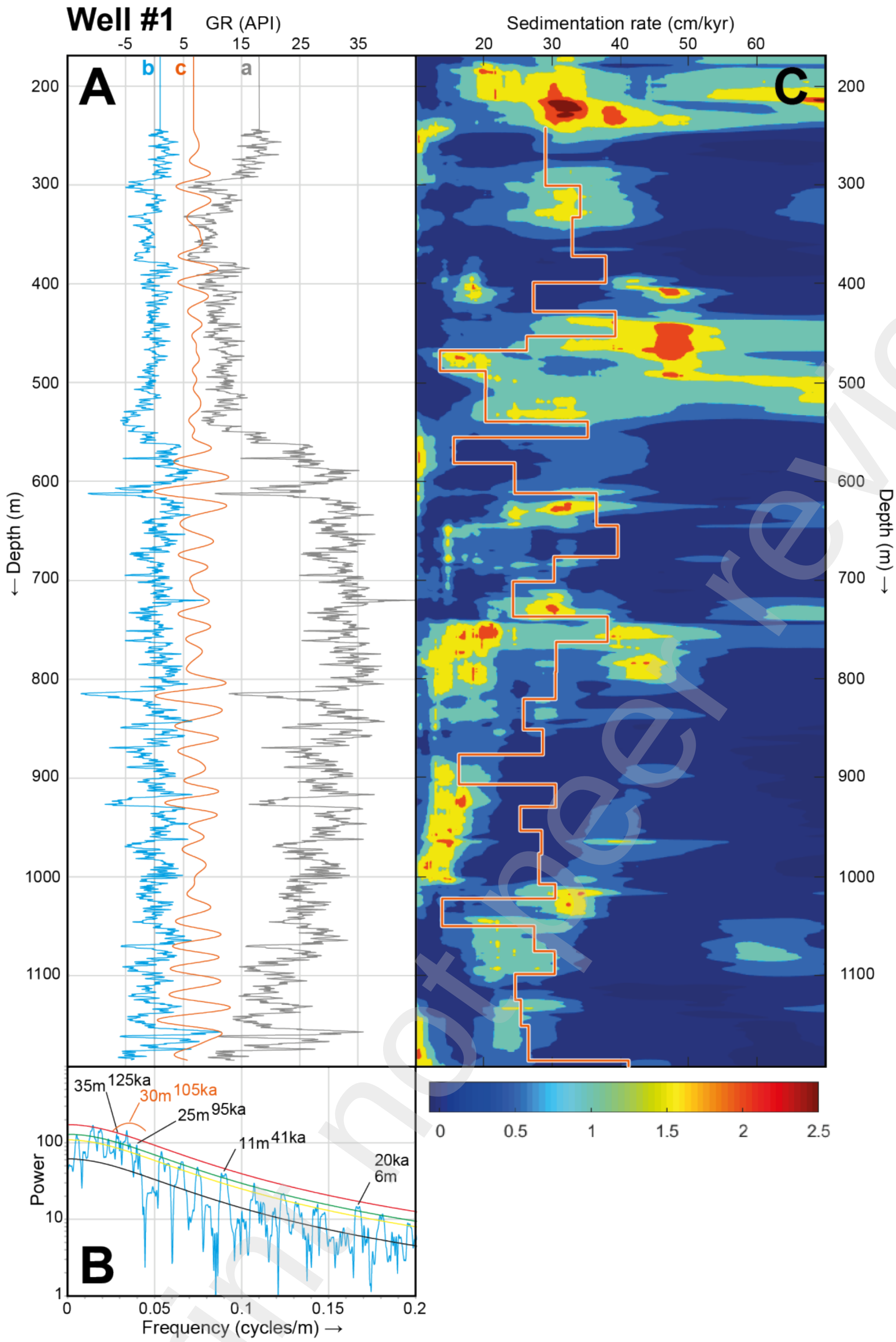

Figure 5: Cyclostratigraphic analysis of GR data of Well #1 along the siliciclastic series (depths 168 to 1194 m Kelly Bushing). (A) Raw GR dataset (Curve a) extended to the seafloor (see Data and Methods). Detrended GR data using a 35% LOWESS regression (Curve b). Bandpass filter output of 25 to 35 m cycle band (0.024 to 0.046 m^{-1}) potentially associated with Earth's short orbital eccentricity (Curve c). (B) 2π-MTM power spectrum of the detrended GR data along with the interpreted orbital cyclicities using manual frequency ratio method. Red, green, yellow and black lines indicate 99%, 95%, 90% and median robust AR (1) red noise confidence levels respectively. (C) eCOCO results compared to the sedimentation rates (orange curve) inferred from a tuning on La2004 Earth short eccentricity.

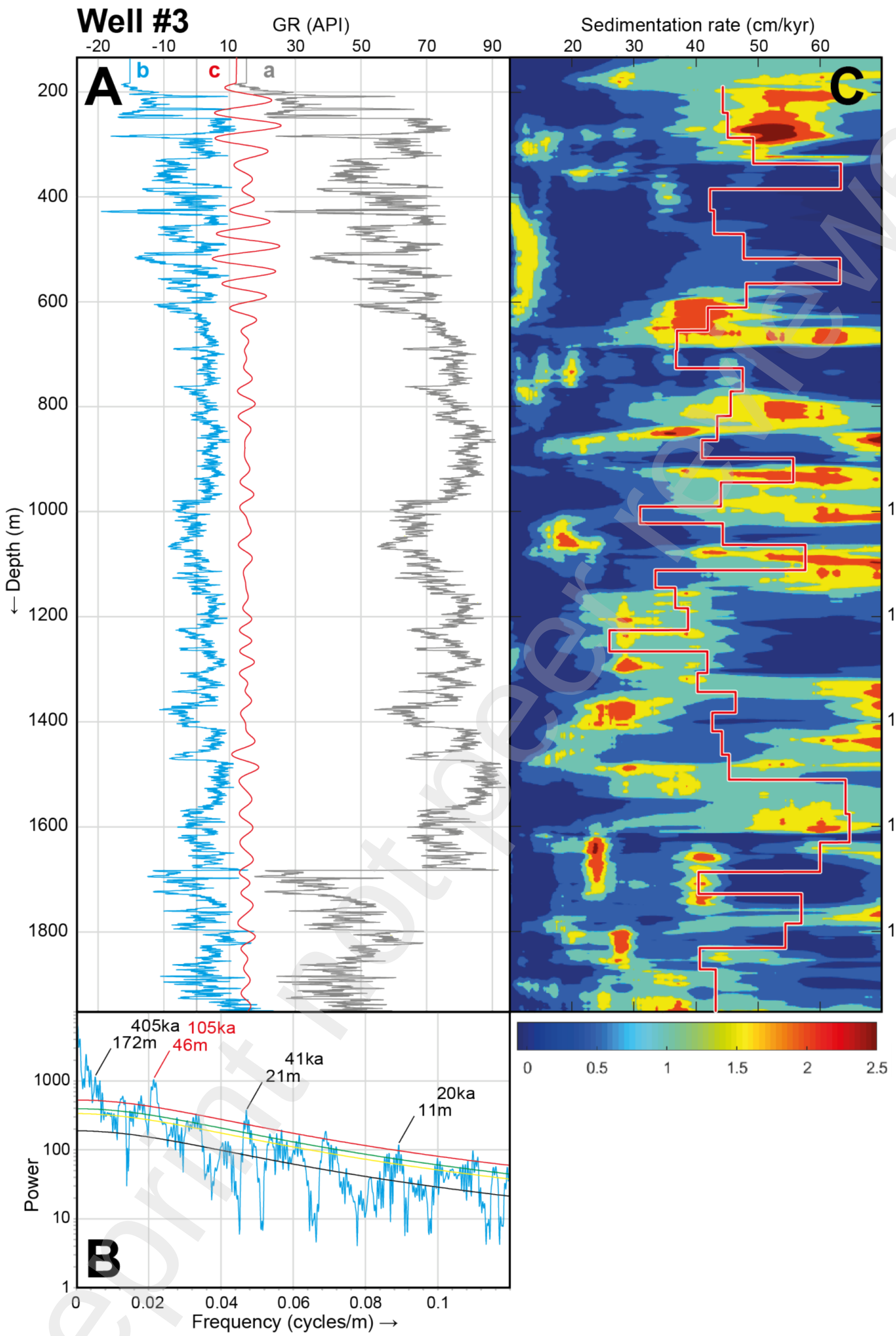

Figure 6: Cyclostratigraphic analysis of GR data of Well #3 along the siliciclastic series (depths 132 to 1954 m Kelly Bushing). (A) Raw GR dataset (Curve a) extended to the seafloor (see Data and Methods). (b) Detrended GR data using a 35% LOWESS regression (Curve b). Bandpass filter output of 46 m cycle band potentially associated with Earth's short orbital eccentricity (Curve c). (B) 2π-MTM power spectrum of the detrended GR data along with the interpreted orbital cyclicities using manual frequency

ratio method. Red, green, yellow and black lines indicate 99%, 95%, 90% and median robust AR (1) red noise confidence levels respectively. (C) eCOCO results compared to the sedimentation rates (orange curve) inferred from a tuning on La2004 Earth short eccentricity.

Two independent age models were constructed for Wells #1 and #3 based on a tuning to La2004 (Laskar et al., 2004) cycle minima of Earth's short eccentricity *(Figure 7*).

The age model of Well #1 indicates an age of the base of the siliciclastic series at 3688 kyr when tuned to the La2004 Earth's short eccentricity (*Figure 7*). The age of each seismic unit boundary correlates more or less with the global sea-level falls inferred from deep-sea foraminiferal $\delta^{18}O$ (Miller et al., 2020; *Figure 7*). The age model of Well #3 suggests an age of the base of the siliciclastic series at 3960 kyr (*Figure 7*). The difference in the basal age of the siliciclastic series, 272 kyr between the two wells, could be attributed to the varying positions of the wells. Well #3, being closer to the Amazon River mouth, may have received sediments earlier compared to the more distant well #1. Significant decreases in GR values are likewise correlated with major falls in the global sea level. Due to the poor quality of the available 2D seismic lines, the limits of seismic sequences could not be accurately extended to Well #3. Nonetheless, significant drops in the GR of Well #3 can potentially be correlated with those in Wells #1 and #2. These significant drops have then been correlated with seismic sequence boundaries on the basis of the time-depth relationship. The offsets between the main sea level falls and seismic sequence boundaries can be explained by tuning to astronomical forcings (*Figure 7*). While astronomical forcings do influence climate, it's important to note that they are not the sole proxy affecting climate, and their effects are not instantaneous.

Each age model allows assessment of sedimentation rates along each well. The manually obtained sedimentation rates were then compared to those inferred from the eCOCO method. The manual sedimentation rates in Wells #1 and #3 capture the general trends of the eCOCO sedimentation rates (*Figures 5 and 6*). Some mismatches have also been noted, which may be explained by abrupt changes in sedimentation rates. Sedimentation rates inferred from both methods exhibit high variability. Along Well #1, sedimentation rates range from less than 15 cm/kyr to up to 40 cm/kyr (*Figure 5*). In Wells #2 and #3 sedimentation rates vary from 18 to 45 cm/kyr and 25 to 65 cm/kyr, respectively (*Figures 6 and S2*). This high variability in sedimentation rates accounts for the multiple frequency peaks observed in the Multi-Taper Method (MTM) spectral analysis (*Figures 5 and 6*). The MTM analysis also reveal a stronger short eccentricity component compared to the obliquity power (*Figure 7*).

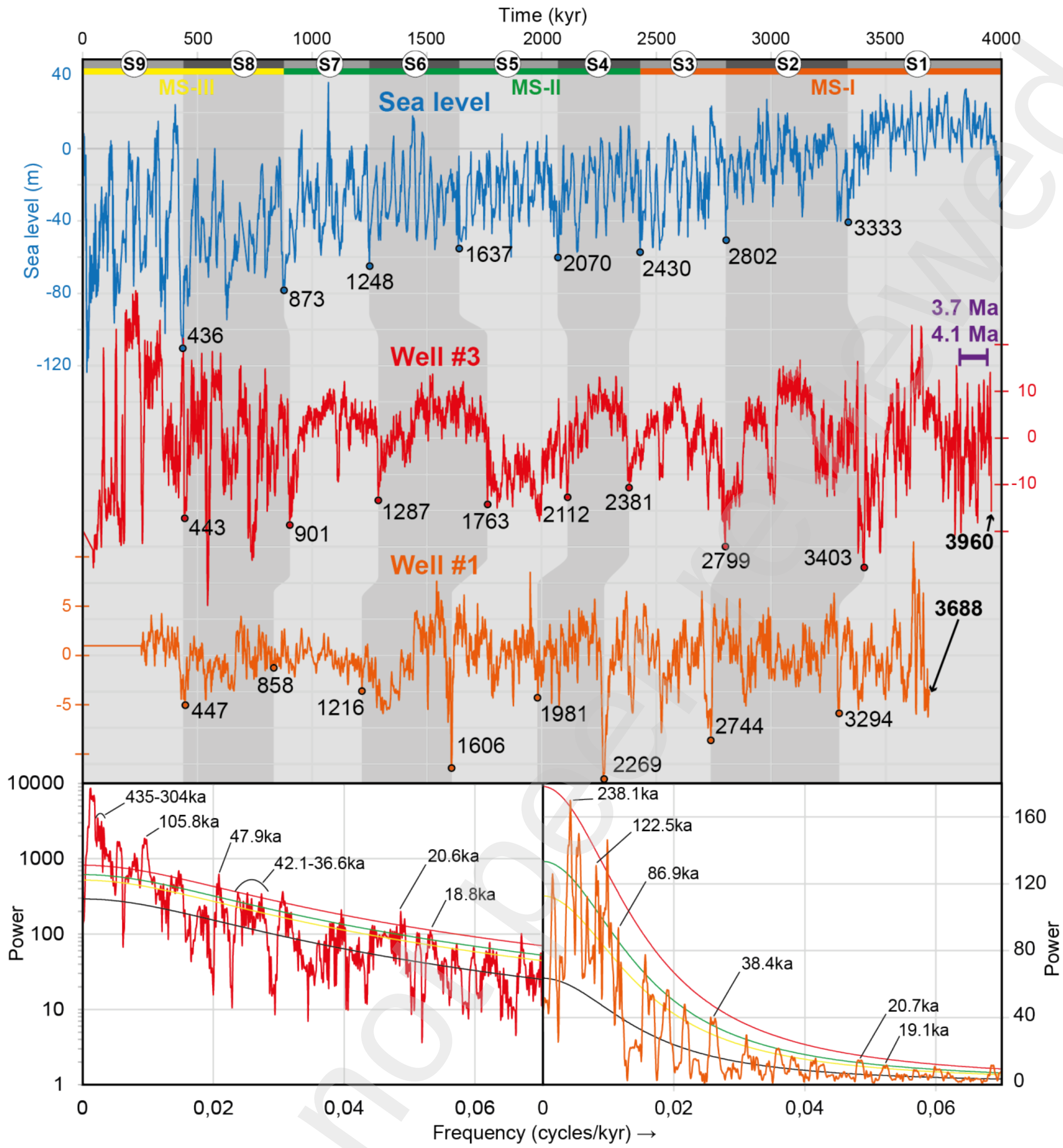

Figure 7: GR data of Wells #1 and #3 in time domain after a tuning between the La2004 Earth's short eccentricity minima and the minima of the filters of 30 m frequencies and 46 m frequencies for Well #1 and #3 respectively. The GR curves in time are compared to sea level variation from Miller et al. (2020). Dark and light grey area behind the curves corresponds to seismic sequences and the potential eustatic cycle associated. The lower panels present the Multi-Taper-Method of Wells #3 and #1 (see corresponding colours), with the main astronomical cyclicities. Red, green, yellow and black lines represent the 99%, 95%, 90% and median Robust AR (1) confidence levels respectively.

4.4. Comparison between seismic observations and cyclostratigraphy

As a first approximation, we can assume that each seismic sequence has developed over the same amount of time and corresponds to the same cycle order. Thus, we divide the duration of the studied siliciclastic series given by biostratigraphy, i.e. 3.7-4.1 Myr, by the number of the observed seismic sequences. We obtain a duration of 411-456 kyr for each of the seismic sequences (9 sequences/3.7-4.1 Ma; *Figure 4*). The 411-456 kyr duration is close to the 405 kyr eccentricity periodicity, suggesting an orbital driver of the major seismic sequences S1 through S9 (Figure 7). This hypothesis is supported by cyclostratigraphy of GR data, and in particular by the presence of 4 short eccentricity cycles (97 to 128 kyr) within each major seismic sequence (*Figure 7*). Additionally, GR data in Well #3 record the 405 kyr eccentricity cycle (*Figures 6 and 7*). Therefore, we conclude that long eccentricity (405 kyr) is the main orbital parameter influencing the sediment architecture on the Amazon continental margin as observed on our seismic data.

Within seismic sequences S8 and S9, nine smaller scale sequences are exceptionally well expressed (FR1 to FR9, *Figure 4*). The seismic sequences (S1 through S9), being associated with long eccentricity cycles (405 kyr), allow to calibrate the smaller scale sequences to a periodicity close to the short eccentricity. We can equally use the age obtained through cyclostratigraphy for the base of Sequence S8 inside Well #1: 858 ka and inside Well #3: 901 ka (*Figure 7*) to calculate the periodicity of these smaller scale sequences. We obtain two periodicities of ~95.3 kyr (858/9) for Well #1 and ~100 kyr (901/9) for Well #3. Finally, GR data of Well #3 document a stronger short eccentricity signal within sequences S8 and S9 matching the smaller scale seismic sequences (*Figure 7*).

5. Discussion

5.1. Orbital forcing of Plio-Pleistocene succession in offshore Amazon Basin

Our results highlight the impact of Milankovitch cycles on the nature and architecture of sediments in the offshore Amazon Basin. In particular, cyclostratigraphic results highlight three main frequency bands related to short eccentricity (97-128 kyr), obliquity (41 kyr) and precession (19-23 kyr). Major seismic sequences are correlated to the 405 kyr eccentricity cycle. (*Figure 7*).

Previous studies of the sedimentary architecture of continental margins using seismic and well-log data have proposed a correlation between depositional sequences and the 405 kyr orbital eccentricity cycles (e.g., (Chima et al., 2020; Gorini et al., 2014). On the Amazon margin, Gorini et al. (2014) proposed that the 405 kyr cycle drove the deposition of clastic sequences overlying the Amapá carbonate platform and proposed a basal age of the siliclastic serie of 2.4 Ma on the area, based on 2D seismic interpretation. Our astronomical age model and our 3D seismic interpretation indicate that the outbuilding of the shelf due to deposition of Amazon-derived clastics began earlier, at around 3.7 Ma (*Figures 7 and 8*).

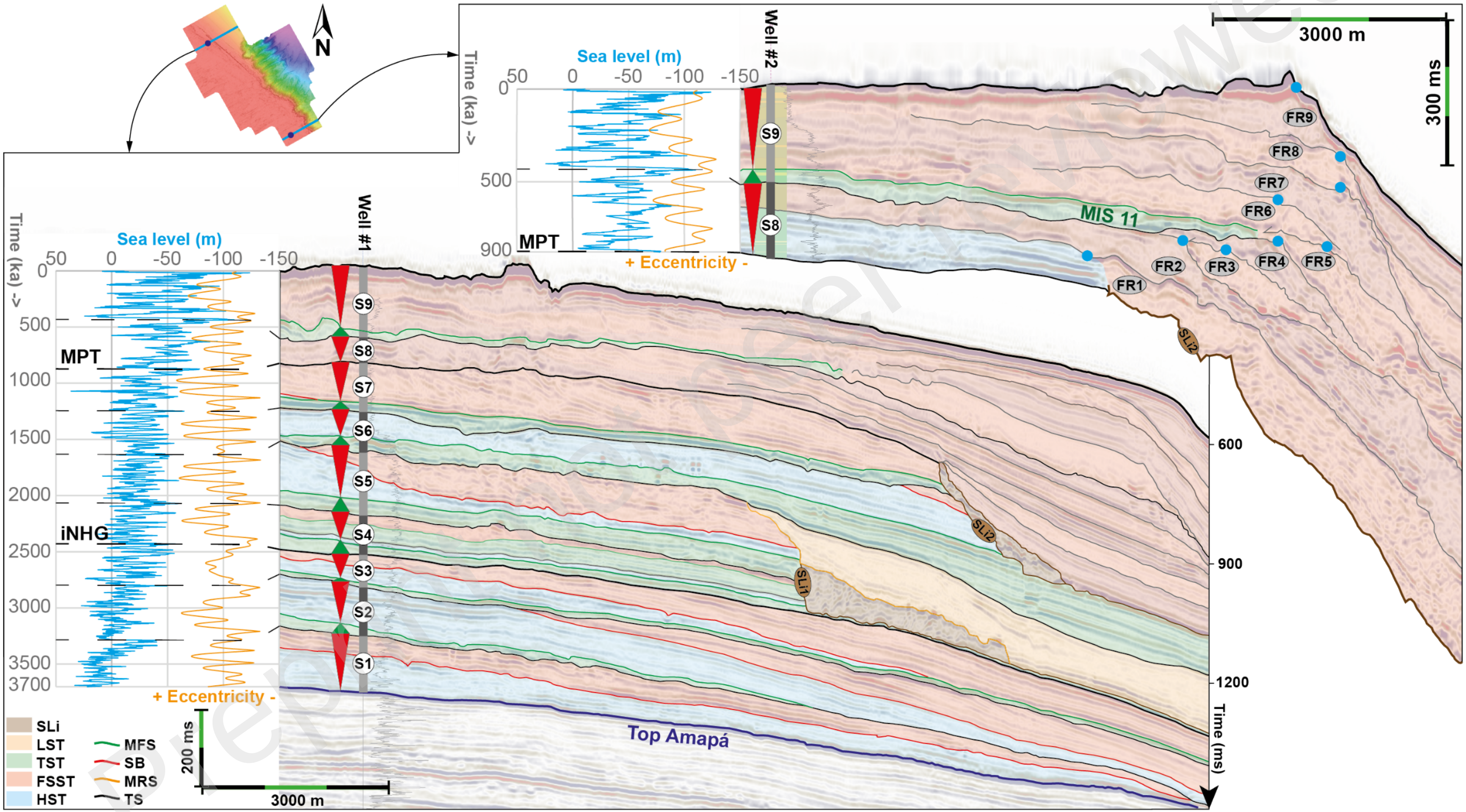

N
Sea level (m)
Time (ka) ->
Well #2
Well #1
+ Eccentricity -
MPT
iNHG
MIS 11
3000 m
300 ms
200 ms
Top Amapá
Time (ms)
SLi
LST
TST
FSST
HST
MFS
SB
MRS
TS

Figure 8: Sequence stratigraphy interpretation of the inlines A and B (see their location in Figure 1). The sea level curve of Miller et al. (2020) is shown on the left side of wells #1 and #2 in light blue. The orange curve represents the Earth's short eccentricity from the La2004 solution. The red and green triangles along the wells depict the relative sea level variation interpreted through seismic observation. Red triangles represent regressions while the green ones transgressions.

In the two youngest seismic sequences (S8 and S9, *Figure 8*), a cyclicity of 100 kyr is proposed and explains the presence of 9 Falling Stage System Tracts or forced regression (FR1 to FR9; *Figure 8*) which are calibrated to the short eccentricity cycle. These forced regressions in the late Quaternary are well known features in many places in the world, e.g. in Mediterranean (e.g. Lobo and Ridente, 2014; Rabineau et al., 2006, 2005; Ridente et al., 2009) or in Gulf of Mexico (Anderson and Fillon, 2004). In Well #3, this cyclicity is apparent in the GR record, and its exceptional preservation could be related to the position of the well closer to the main depocenter of the Amazon deep-sea fan (*Figure 1*). Indeed, the flexural deformation of the lithosphere associated to the deep-sea fan loading can be recognized by changes in the rate of subsidence in the adjacent areas and an increased accommodation space favourable to the aggradation and preservation of shelf-edge deltas (Cruz, 2018; Neal W. Driscoll and Karner, 1994; Rodger et al., 2006; Silva et al., 1998).

Our study also indicates that lithological variation along the offshore Amazon Basin is mainly influenced by short eccentricity (97-128 kyr) as depicted by the MTM analysis (*Figure 7*). This contrasts with the widely accepted idea that obliquity is the main parameter influencing the Earth's climate prior to the Mid-Pleistocene Transition (0.7-1.2 Ma) (Raymo et al., 1997). This difference could be explained by the location of the study area close to the equator, a latitude more sensitive to precession-eccentricity forcing (Berger and Loutre, 1994). Therefore, astronomically driven climate is the dominant mechanism influencing the sedimentation pattern in the study area, whereas the flexural subsidence likely remains the main factor preserving the higher frequency climatic variations recorded in the deltaic sequences of the Amazon margin (Cruz, 2018; *Figure 8*).

5.2. The age of the Plio-Pleistocene Amazon River siliciclastic series

Mega-sequence MS-I is bounded at its base by the transition from Amapá carbonate sediment to clastic sediments from the Amazon River, i.e. the base of the Plio-Pleistocene Amazon River series. We suggest an age of ~3.7 Ma for this transition based on cyclostratigraphy of Well #1 (*Figure 7*). Further south in Well #3, the basal age of the Plio-Pleistocene series shows an older age of 4 Ma (*Figure 7*). This diachroneity of the basal age of the Plio-Pleistocene series is consistent with the study of Cruz et al. (2019), who showed that the age of carbonates demise decreased northward across the offshore Amazon Basin, with a longer carbonate growth towards the north, and therefore a younger age of cessation. This result is also consistent with the observation of NE migration clinoforms by Gorini et al. (2014), which cover the Amapá carbonate platform. This concurs with our results revealing a 10 m thick layer of sandy sediments covering the last occurrence of Amapá carbonates (*Figure 2*). This sandy unit is covered by a Highstand System Tract (HST), consisting of muddy bottomsets of delta-scale subaqueous clinoforms downlapping the previous surface (*Figure 8*).

5.3. Correlation of seismic mega-sequences to climate and sea-level changes

Here, we suggest to correlate major stratigraphic changes observed in seismic geometries and dated by cyclostratigraphy, with trends in global sea level (Miller et al., 2020).

Within MS-I, the first identified Falling Stage System Tract (FSST) inside the seismic sequence S1 is probably associated with a climatic change between 3.5 to 3.3 Ma and a global sea level fall (Mammoth 2 event or MIS M2; (De Schepper et al., 2013). During Sequence 1 (S1), the main sea level fall is fast with high amplitude (60 m in 100 kyr; Miller et al., 2020). During this time span, FSST observations reveal clear migration of the coastline towards the basin with a large (marine) erosional surface at its base. Seismic Sequence 2 (S2) corresponds to a period of relatively high sea level defined by the development of a HST that lasts from 3.3 to 3.0 Ma based on the cyclostratigraphic age model. This time interval matches the timing of the Mid-Pliocene warm period, ranging from 3.264 to 3.025 Ma (Dowsett and Caballero Gill, 2010; Haywood et al., 2009). This interval is recorded as a thick aggrading and prograding Highstand System Tract (HST) inside S2 (*Figure 8*). This warm period is followed by a cooling event and a long duration of sea level fall (from 3.0 to 2.8 Ma; Miller et al., 2020). The third FSST inside S3 corresponds to a global sea level fall standing from 2.75 Ma to 2.51 Ma with an amplitude of almost 80 m (Miller et al., 2020). Even if it represents the strongest sea level fall, it is also the longest in duration (320 kyr), thus implying a very low rate of sea level fall. This explains the well-developed FSST, with a larger volume of sediments than in the previous two FSST.

The transition from MS-I to MS-II is dated at 2.4 Ma according to cyclostratigraphy, which could be related to the intensification of Northern Hemisphere Glaciation (iNHG) around 3.0 to 2.5 Ma (Bartoli et al., 2005; Kleiven et al., 2002; Maslin et al., 1998; Wohlfarth et al., 2008). The thickness and volume of the FSST and TST are greater during MS-II than MS-I which might be correlated to higher sedimentation rates. The increased sedimentation rates may be due to enhanced erosion since the iNHG, due to enhanced Andean glaciation and variation in precipitation on the Amazon drainage basin during colder glacial stages (Harris and Mix, 1999; Mason et al., 2019). This change is also observed in pollen data (at 2.6 Ma), transition between Zones C to D as described by Hoorn et al. (2017). During MS-II (2.4 to 0.9 Ma), Transgressive System Tracts (TST) are more developed and we correlated the first two with sea level rise events from 2.5 to 2.2 Ma (MIS 95-91, Lisiecki and Raymo, 2005) and from 1.64 to 1.44 Ma (MIS 57-47, Lisiecki and Raymo, 2005). The last Transgressive System Tract observed in S7 is probably associated with MIS 31 (1.07 Ma, Lisiecki and Raymo, 2005).

During MS-III (0.9 to present-day), the shape of the FSST changes drastically as well as their location along the passive margin (*Figure 8*). This could be explained by the variation of the dominant orbital parameter on the climate. Indeed, after the MPT, the Earth is dominated by 97-128 kyr cyclicity and sea level variation has increased dramatically (Berger and Loutre, 1994; Chalk et al., 2017; Clark et al., 2006; Pisias and Moore, 1981; Willeit et al., 2019). This may have led to the expression and preservation of the shorter seismic sequences forced by the short eccentricity. The successive drops in sea level related to successive glacial stages may have led to high variation of the coastline position resulting in regressive prisms along the slope (forced regression). Indeed, the available space for sediments is considerably reduced on the outer shelf during strong sea level falls and the sediments migrate towards the slope. During the S8 seismic sequence, the FSSTs mainly prograde and the aggradation remains very low (*Figure 8*). However, during seismic sequence S9, aggradation dominates progradation. This correlates with the Mid-Brunhes transition, which shows over the last 405 kyr, interglacial stages with warmer temperatures (Jouzel et al., 2007), and an overall increase in the mean sea level (Barth et al., 2018; Mitsui and Boers, 2022). This causal link between FSST and the short eccentricity (97-128 kyr) after the Mid-Pleistocene Transition has also been observed in other deltas (Lafosse et al., 2018; Rabineau et al., 2006). The FSSTs are also accompanied by an increase in erosion rates. Indeed, during low sea levels, the shoreline can reach the outer shelf and most of the shelf could then be exposed to aerial erosion. During transgression, patch reef extensively grew around the outer shelf on top of the shelf edge deltas (forced regressions). During S8-S9 transition, we observed an increase in carbonate production that we relate to the MIS 11 climatic event at 0.45 Ma (Droxler and Jorry, 2021).

5.4. Subsidence: a vital factor for preservation

The record of the complete Milankovitch cycle bands, short eccentricity, obliquity and precession reveals the good preservation of the sedimentary deposits on the north-western Brazilian Equatorial margin. Indeed, most stratigraphic sequences seem to be preserved with limited seismic evidence of erosion. Such good preservation is only possible through subsidence. Two types of subsidence affect the Brazilian equatorial margin (Bott, 1992): thermal subsidence due to post-rift (<100 Ma) cooling; and sediment loading by the Amazon fan since 8 Ma, which can be 10 times higher.

We can calculate this total subsidence rate around Well#1 with simple approximations. If we consider that the top of Amapá formation is at 0m water-depth, as well as the top of S9 at MIS2 (20 ka). We measure a thickness of sediment deposition of 1090 m. Therefore, we obtain an average total subsidence rate of: 1090m deposited in (3.7 – 0.02) = ~300 m/Myr. This value is rather high, but has been observed on other margins in the world (e.g. in the Mediterranean Sea: Rabineau et al., 2014) and is, in fact, a pre-conditioning factor for the record of Pliocene and Quaternary high resolution sequences on the shelf. The same calculation on Well#3 leads to an average subsidence rate of: 1822m/4 Ma = ~450m/Myr. Note that Well #2, which is in between, well #1 and well#3 shows an intermediate subsidence rate of ~375m/Myr. Therefore, the variations between the northern and southern geometries can be explained by differential subsidence rate.

6. Conclusions

This study provides new results on the possible effects of climate variations on the architecture of Plio-Quaternary sedimentary deposits along the Brazilian Equatorial Margin influenced by terrigenous inputs. A 3D seismic sequence stratigraphic study reveals 3 mega-sequences and 9 seismic sequences, deposited during the last 3.7-4.1 Ma based on biostratigraphic data from wells. A cyclostratigraphic analysis of gamma ray data in 3 wells yields an orbital age model in which the seismic sequences are tied to the 405 kyr eccentricity cycle. The first mega-sequence (MS-I) is dated between 4.0 to 2.4 Ma and its characteristics are interpreted to record sea level variations of low amplitudes (~40 m), preceding the intensification of Northern Hemisphere Glaciation. The second mega-sequence (MS-II) is dated at 2.4-0.9 Ma and is characterized by the development of major erosional surfaces and an increase in the slope of clinoform forests. This change in the overall geometry of the shelf is potentially due to an increase in the amplitude of sea level variations coupled with an intensification of the erosion rate within the Amazon basin. The third mega-sequence (MS-III) is dated at 0.9-0 Ma and is characterised by nine lowstand prisms, of which the oldest five are prograding, while the youngest four become aggrading. The orbital age model allows to ascribe these prisms to the short eccentricity. The abundance of lowstand packages is related to a change in the orbital forcing regime at the Mid-Pleistocene Transition. Moreover, ~405 kyr ago during MIS 12-11 transition, the average temperature of the Earth increased, raising the average sea level and allowing the lowstand prisms observed in the seismic record to become aggrading. Correlation with the global sea level curve indicates that the 9 prisms within MS-III correspond to glacial-interglacial cycles and correlate with MIS 6, 8, 10, 12, 14, 16, 18, 20 and 22. In summary, the sedimentary architecture of the North-western Brazilian Equatorial Margin records significant changes in its overall geometry at 2.4 Ma, 0.9 Ma and 0.4 Ma due to the intensification of Northern Hemisphere Glaciation, the Mid Pleistocene Transition and the Mid-Brunhes Transition, respectively. The good record and preservation of these climate-related sequences is due to a significant total subsidence rate in the area of ~300m/Ma on the outer shelf. We related this important subsidence rate to the loading effect of the Amazon deep-sea fan.

Declaration of interests

The authors declare that they have no known competing financial interests or personal relationships that could have appeared to influence the work reported in this paper.

Acknowledgments

This work was supported by the “Region Bretagne” as well as ISblue project: Interdisciplinary graduate School for the blue planet (ANR-17-EURE-0015) and co-funded by a grant from the French government under the program "Investissements d'Avenir" embedded in France 2030. This project was supported by the Region Bretagne and UMR6538 Geo-Ocean joint Unit (CNRS, Univ Brest, Ifremer, Univ. Bretagne Sud). Lucas Tortarolo was a PhD student at “Université de Bretagne Occidentale (UBO, Univ Brest)” and Sorbonne University (SU) in France and was in joint supervision with “Universidade Federal Fluminense (UFF)” in Brazil. This project is also a collaboration with the “Faculdade de Oceanografia” (UERJ) located in Brazil. Lucas Tortarolo is currently employed by the ELIIS company, which developed the software used for creating maps for the 3D geomorphological interpretation of 3D seismic data.

Antonio Tadeu dos Reis also thanks “CNPq” and “FAPERJ” for the research grants (process #309779/2021-9 and process #200.427/2023, respectively). Cleverson Guizan Silva acknowledges “CNPq” for the research grant 311589/2022-7. Slah Boulila was supported by the French Agence Nationale de la Recherche (ANR-19-CE31-0002 AstroMeso), and the European Research Council (ERC) under the European Union’s Horizon 2020 Research and Innovation Program (Advanced Grant AstroGeo-885250).
This work employed Artificial Intelligence to correct and enhance the writing. The following prompt was utilized for this purpose: "Proofread my writing. Fix grammar and spelling mistakes. And make suggestions that will improve the clarity of my writing".

7. Supplementary contents

7.1. Supplementary Figures

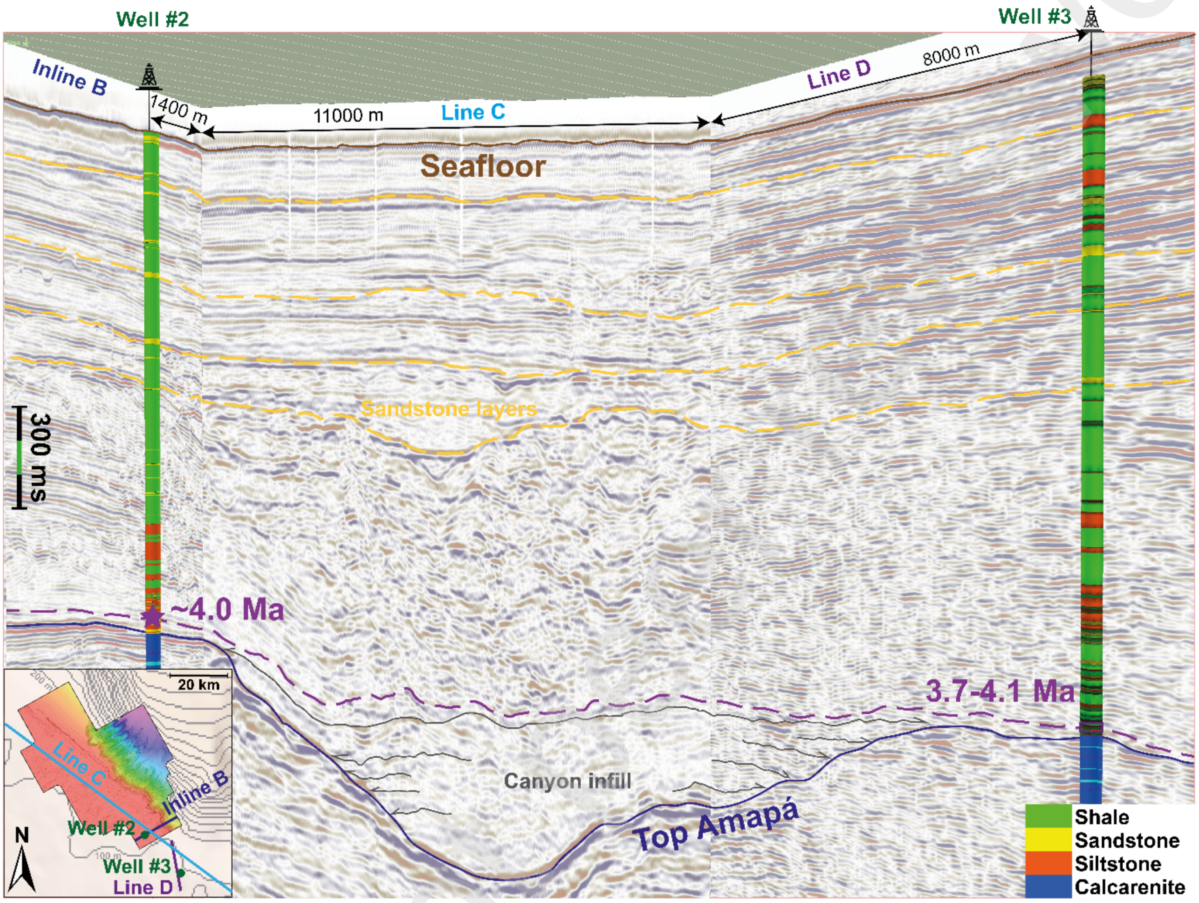

Figure S1: 3D seismic viewer revealing the correlation used to propagate the biostratigraphic age from Well #3 to the seismic block through two 2D seismic lines named C and D. The small box in the bottom left shows the position of the different lines and wells compared to the seismic block position. The top of Amapá is eroded by a major canyon avoiding an easy propagation. However, the bottom part of the canyon is fulfilled by reflectors with onlapping terminations noted canyon infill in the figure. While the upper part shows easy to propagate and correlate sandy layers which are highlighted in yellow. The position of the samples used for biostratigraphy correspond to the first set of reflectors which covers the canyon and the adjacent shelf (purple dashed line).

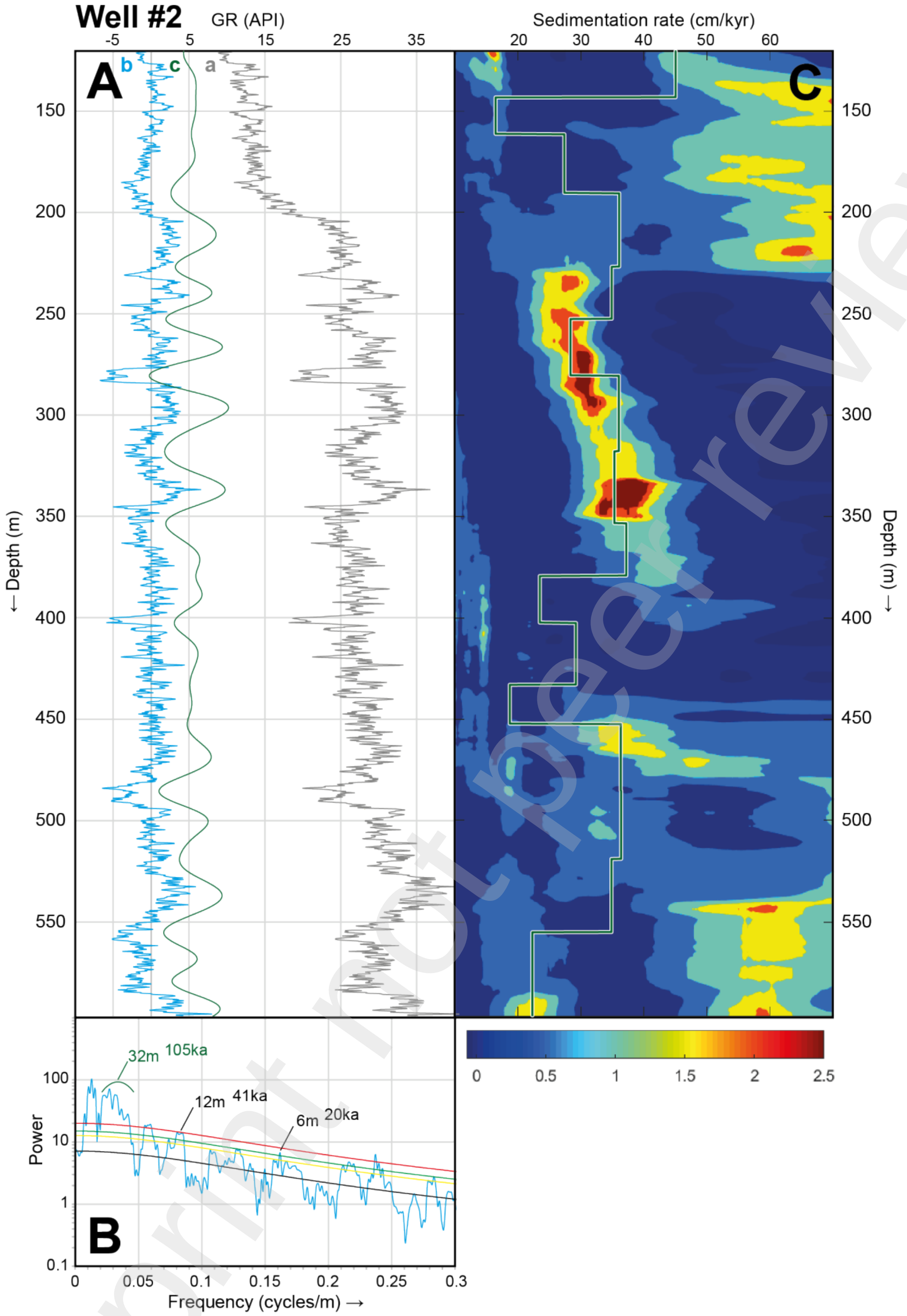

Figure S2: Cyclostratigraphic analysis of GR data of the upper non-deformed interval of Well #2 (depths 120 to 596 m KB, upper siliciclastic series). (A) On the left-side panel: (a) Raw GR dataset. (b) Detrended GR data using a 35% LOWESS regression. (c) Bandpass filter output of 32 m cycle band potentially associated with Earth's short orbital eccentricity. (B) The lower panel shows 2π-MTM power spectrum of the detrended GR data along with the interpreted orbital cyclicities using manual frequency ratio method. Red, green, yellow and black lines indicate 99%, 95%, 90% and median robust AR (1) *red noise confidence levels respectively. (C) The right-side panel shows eCOCO results compared to the sedimentation rates (orange curve) inferred from a tuning on La2004 Earth short eccentricity.*

7.2. Cyclostratigraphy methods

The cyclostratigraphic method is based on gamma ray (GR) well-log data. GR variations in geological formations are connected to the concentrations of radioactive atomic nuclei, mostly uranium, thorium and potassium, which in general are higher in shale and clay intervals than sandy sediments, and very low in limestones. Therefore, GR logs are a good proxy for lithological variations in a siliciclastic and mixed siliciclastic-carbonate sedimentary environments. In shelf settings, sediment sorting is mostly related to variations in ocean energy, which to a first approximation decrease seaward. Thus, GR well log data can provide a reliable proxy of distance from the shore during sea-level variations (Merkel, 1979). GR well log data has already been used as an indirect paleoclimatic proxy to characterize orbitally-driven sea level variation (e.g. Ruffell and Worden, 1999; Weedon et al., 2004; Wu et al., 2013).

To correlate well logs to seismic data in the time domain, downhole check-shots were used and an additional statistical wavelet was created on Paleoscan Software. A more accurate deterministic wavelet could not be generated due to the lack of geophysical well log data from the Plio-Pleistocene succession. The time-depth relationship therefore has an uncertainty estimated at 30 m, except for certain lithological transitions, e.g., from Amapá carbonates to overlying siliciclastics, which are well defined in both the well and seismic data.

Various age models have been developed for wells #1, #2, and #3, all employing cyclostratigraphy based on gamma-ray (GR) data. Here after, we present distinct methodologies that lead to age models with highly comparable results.

7.3. Age model based on intervals

7.3.1. Method

The GR data have been subdivided into different intervals based on sequence stratigraphy. This subdivision allows reducing the effects of variations in sedimentation rate on the record of sedimentary cycles. Along Well #1, we decided to use the limits of the seismic sequences as well as the important variations of GR as limits of our intervals. The sharp changes of GR directly result from a variation of lithology (and therefore acoustic impedance) and are thus well visible in seismic reflection (since great variations of acoustic impedance results in increased seismic wave reflection). In the case of Well #2, we decided to use the same GR intervals as in Well #1. To do this, we extended the limits of these intervals via the 3D seismic block using horizons constructed by Paleoscan. Lastly, as Well #3 is located outside the block, we could not use a similar method. We decided, therefore, to use only the significant GR drops as interval boundaries. However, we relied on a visual correlation between wells to get the most similar cut-off possible across available wells.

The astronomical time calibration (or tuning) was done on the short (100 kyr) eccentricity cycle because it is well expressed throughout the Plio-Pleistocene series. We first established a floating timescale based on a pure 100 kyr periodicity. Then, the 100 kyr tuned GR was anchored at minima of the 405 kyr eccentricity cycles, based on the La2004 astronomical model (Laskar et al., 2004) assuming that some major shifts in GR match boundaries of prominent seismic sequences. Finally, we correlated the absolute-age tuned GR to the La2004 raw eccentricity, and checked the validation of our age model by considering the available biostratigraphic data at Well #3 (Cruz et al., 2019).

7.3.2. Results

Well #1

The MTM spectral analysis performed per intervals on GR data (*Figure S3*) shows two to three distinct peaks of frequency ratios close to the short eccentricity, obliquity and precession. The strongest peak for each interval corresponds to the short eccentricity cycle (97-128 kyr). In most of the intervals, the two other peaks match the obliquity (41 kyr) and precession (19-23 kyr). The short eccentricity wavelength ranges from 17 to 45 m, pointing to a significant change in sedimentation rate through Well #1. The COCO results further support the manual frequency ratio method (*Figure S4*).

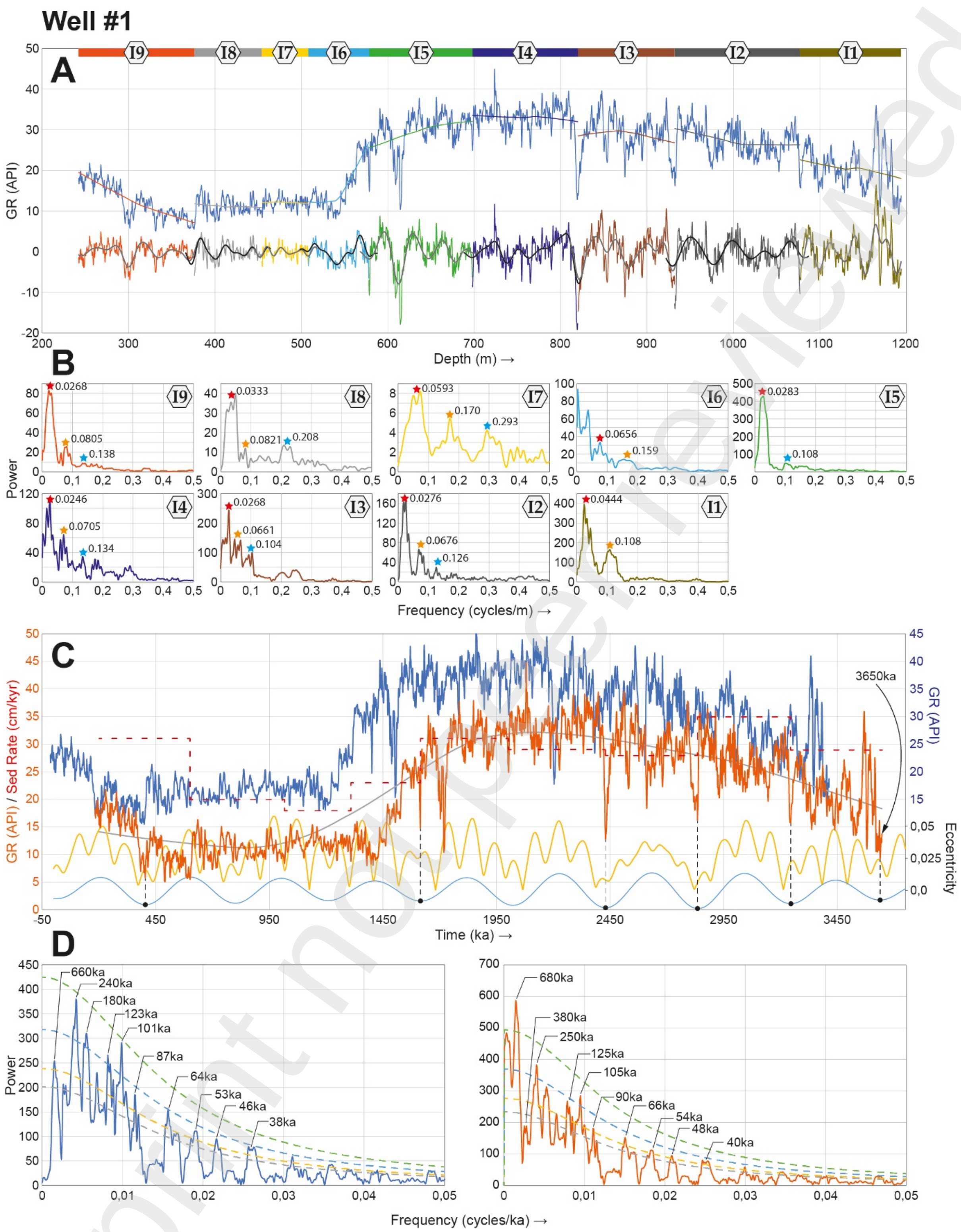

Figure S3: Cyclostratigraphic analysis of GR data of Well #1 (depths 242 to 1194 m, Plio-Pleistocene section). (A) Raw and detrended GR data along with the analysed stratigraphic intervals (labelled I1 through I9 from the oldest to the youngest). The filtered wavelength of the short eccentricity is also shown along with the detrended data. (B) 2π-MTM power spectra of the detrended stratigraphic intervals (mentioned by the color codes). Red, orange and blue stars on spectral peaks indicate possible short eccentricity, obliquity and precession related wavelengths. (C) The 100 kyr tuned GR data (blue:

tuned to a pure 100 kyr sine curve, orange: the 100 kyr tuned GR curve is anchored to 405 kyr eccentricity cycle minima) along with the raw La2004 eccentricity data (yellow curve) and the filtered 405 kyr cycle band (light blue curve). The red-dashed curve depicts sedimentation rate inferred from the 405 kyr anchored curve. (D) 2π-MTM power spectra of the tuned GR data to a pure 100 kyr sine (in blue) and those retuned to 405 kyr cycle minima (in orange), along with the robust red noise levels (median, 90%, 95% and 99% confidence levels).

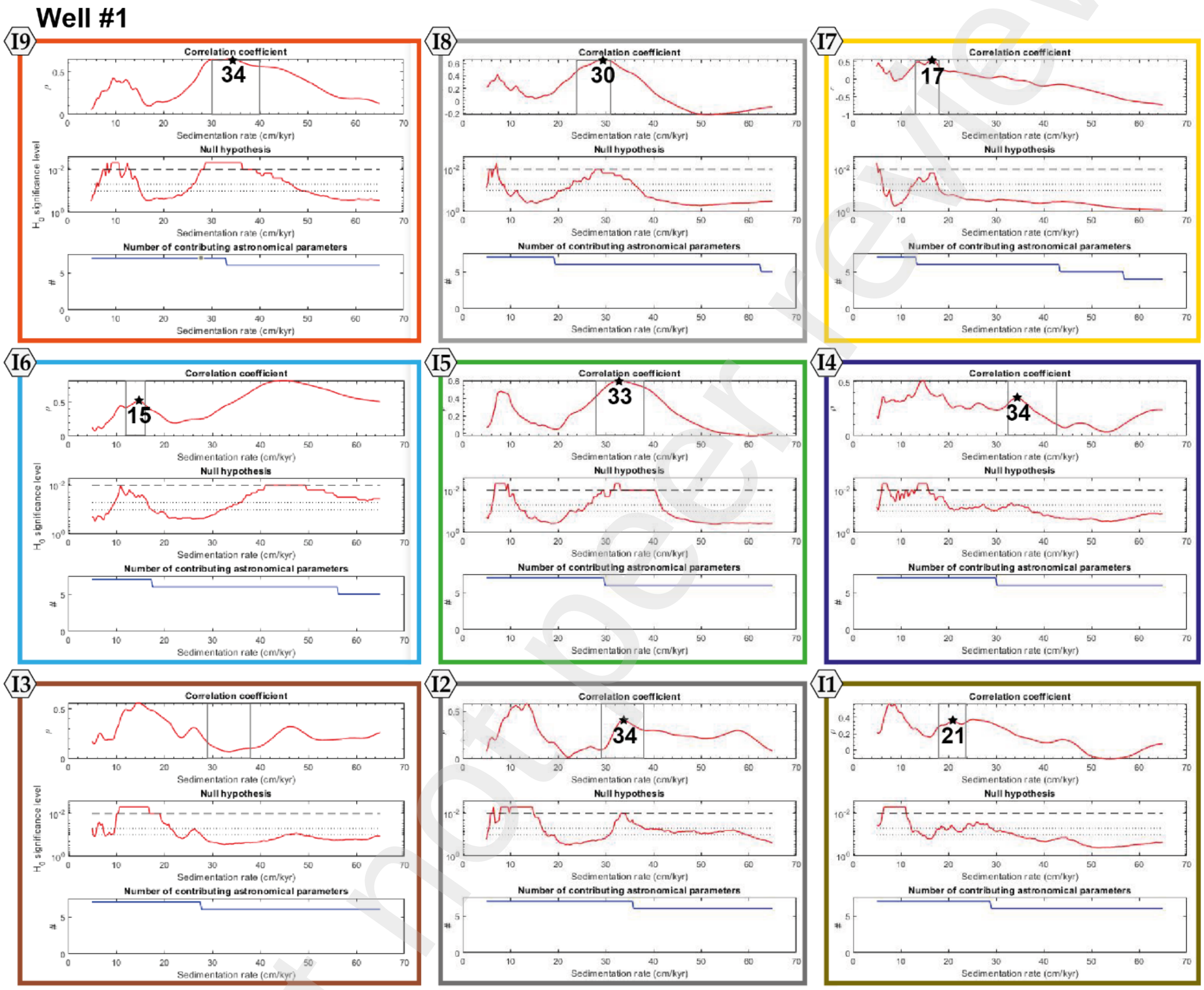

Figure S4: COCO results for each interval of the Well #1 compared with the sedimentation rates obtain through manual frequency ratio methodology. The calculation of sedimentation rate through manual frequency ratio method is represented by the black boxes in each interval. The black stars highlight the most probable sedimentation rate obtain with the comparison with both methodologies and the number is in cm/kyr.

The interval 7 reveals a similar pattern within the three wells. The amplitude of the peak corresponding to short eccentricity cycle (see the vertical axis entitled "power" in the *Figures 4.8.1, 4.8.3 and, 4.8.5* for the interval 7; I7) decreases drastically by at least one order of magnitude making the other two cycles, related to obliquity (41 kyr) and precession (19-23 kyr), comparatively stronger (*Figures 4.8.1, 4.8.3 and, 4.8.5*). While the next two intervals (I8 and I9) contrast with a peak corresponding to short eccentricity parameter (97-128 kyr) with a power 5 to 20 times greater than in I7 (*Figures 4.8.1, 4.8.3 and, 4.8.5*). Interval 4 in the wells (*Figures 4.8.1, and 4.8.5*), shows the same pattern with a decrease in the power of short eccentricity and an increase in precession and obliquity comparatively to adjacent intervals.

The 100 kyr tuning of the whole GR data (*Figure S3*) yields a duration of 3.4 Ma for the Plio-Pleistocene series in Well #1. The MTM spectral analysis of the tuned GR time series (*Figure S3*) reveals several peaks at 660, 240, 180, 123, 101, 87, 64, 53, 46 and 38 kyr. Then, we retuned the 100 kyr GR time series to the 405 kyr eccentricity cycle assuming that their minima correspond to the sharp drops in GR which correlate to boundaries of seismic sequences and major changes in the lithology.

Anchoring the 100 kyr floating time scale to the 405 kyr eccentricity minima allows an absolute age model for Well #1 (*Figure S3*). The MTM spectral analysis of this tuned dataset detects peaks of 125, 105, 90, and 40 kyr (*Figure S3*). The inferred sedimentation rate curve reveals lower values of 20, 18 and 23 cm/kyr for intervals I8, I7 and I6 respectively (from 0.6 to 1.5 Ma), and greater values of 31 cm/kyr and 35 cm/kyr for respectively I9 and I2 (*Figure S3*). In the *Figure S8*, we compare the sedimentation rates inferred from the 100 kyr tuned GR curve with the sedimentation rates estimated with the "eCOCO" approach. We observe an overall good correlation between the two method outputs, further supporting our cyclostratigraphic interpretation based on the manual frequency ratio method. Finally, we obtained an age for the first appearance of Amazon-related terrigenous sediments of 3.65 Ma in Well #1 (*Figure S3*).

Well #2

Within the Plio-Pleistocene series of Well #2, only its upper part is tectonically undeformed (*Figure 4.4*). Thus, we focused on cyclostratigraphy of its upper part (*Figure S5*). We extended the seismic intervals created within Well #1 using 3D seismic to separate the GR data of Well #2 with the same intervals (Intervals I6 through I9; *Figure S5*). The MTM spectral analysis of these intervals (*Figure S5*) shows two to three relevant GR peaks, with elevated power (*Figure S5*). The frequency ratio method allows attributing each of the three peaks, from the lowest to the highest frequency, to short eccentricity, obliquity and precession (*Figure S5*). The COCO results further support the manual frequency ratio method (*Figure S6*). The 100 kyr tuning of Well #2 (*Figure S5*) yields a duration of 1.67 Myr for the upper part of the Plio-Pleistocene series. Finally, the 100 kyr tuned GR data were anchored to the minima of 405 kyr eccentricity cycles (*Figure S5*). The MTM spectral analysis of the 100 kyr tuned GR time series is almost identical to the 405 kyr retuned GR time series. Therefore, only the MTM of the 405 kyr retuned GR is presented (*Figure S5*). It reveals cycles of 440, 250, 116, 100, 55 and 38 kyr. The estimated sedimentation rate from tuning shows lower values of 20 cm/kyr, within interval I7 (from 0.8 to 1.2 Ma), and a higher value of 40 cm/kyr within Interval I9. Results of the "eCOCO" method reinforce the obtained sedimentation rates from the 100 kyr tuned GR data, with possibly one exception at the transition from Interval I7 to Interval I8 where the eCOCO fails in the detection of the optimal sedimentation rates (*Figure S9*). However, the COCO method applied per intervals (I7 and I8) highlight significant optimal sedimentation rate, especially within I8 (*Figure S6*).

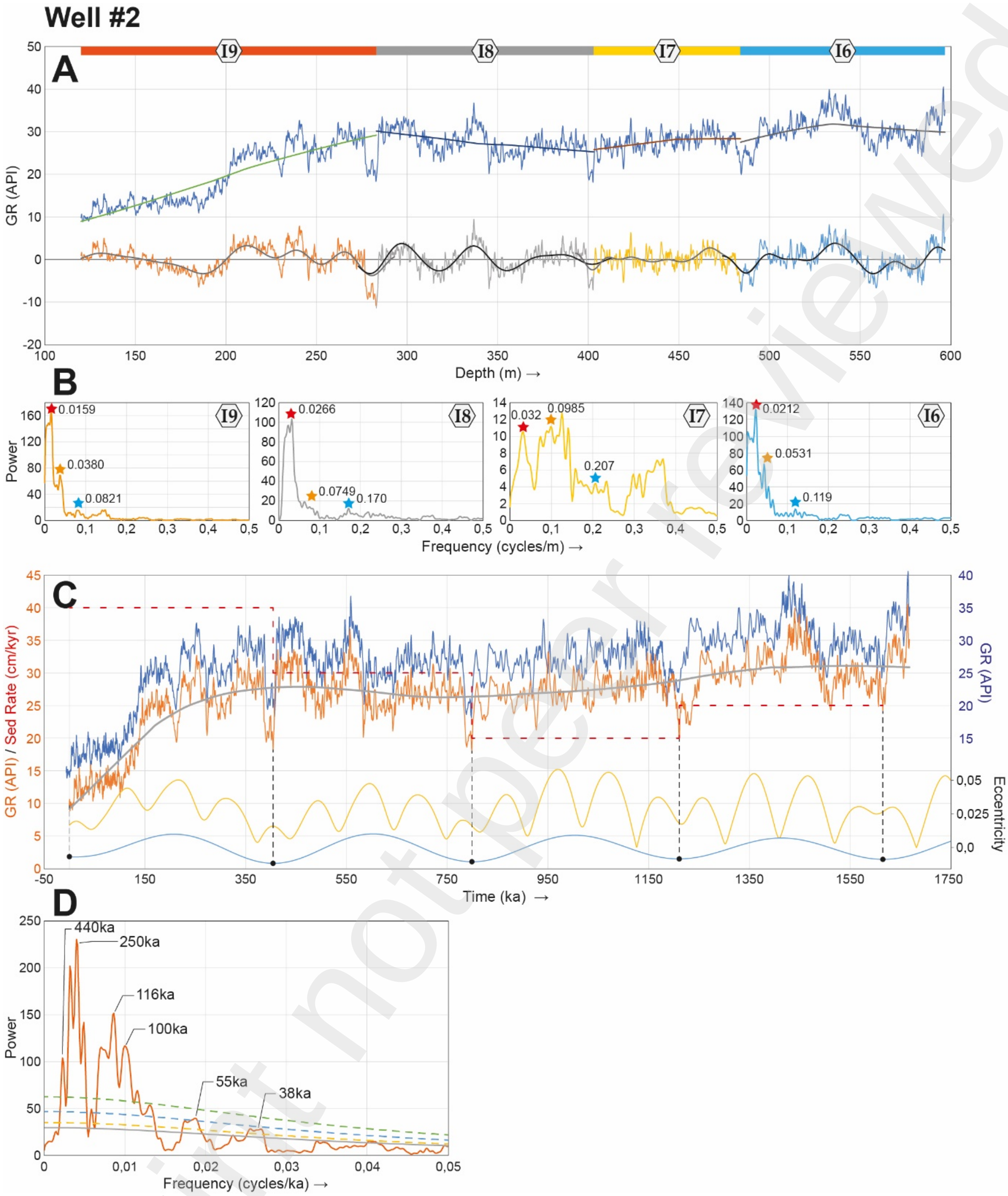
Well #2
A
I9
I8
I7
I6
GR (API)
Depth (m) →
B
0.0159
0.0380
0.0821
0.0266
0.0749
0.170
0.032
0.0985
0.207
0.0212
0.0531
0.119
Power
Frequency (cycles/m) →
C
GR (API) / Sed Rate (cm/kyr)
GR (API)
Eccentricity
Time (ka) →
D
440ka
250ka
116ka
100ka
55ka
38ka
Power
Frequency (cycles/ka) →

784

Figure S5: Cyclostratigraphic analysis of GR data of Well #2 (depths 120 to 596 m, upper Plio-Pleistocene section). (A) Raw and detrended GR data along with the analysed stratigraphic intervals (labelled I6 through I9 from the oldest to the youngest). The filtered wavelength of the short eccentricity is also shown along with the detrended data. (B) 2π-MTM power spectra of the detrended stratigraphic intervals (mentioned by the color codes). Red, orange and blue stars on spectral peaks indicate possible short eccentricity, obliquity and precession related wavelengths. (C) The 100 kyr tuned GR data (blue: tuned to a pure 100 kyr sine curve, orange: the 100 kyr tuned GR curve is anchored to 405 kyr eccentricity cycle minima) along with the raw La2004 eccentricity data (yellow curve) and the filtered 405 kyr cycle band (light blue curve). The red-dashed curve depicts sedimentation rate inferred from the 405 kyr anchored curve. (D) 2π-MTM power spectra of the anchored GR data to 405 kyr cycle minima (in orange), along with the robust red noise levels (median, 90%, 95% and 99% confidence levels).

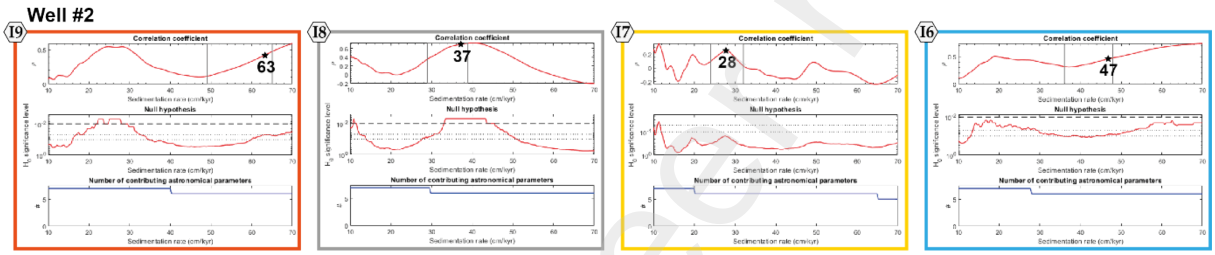

Figure S6: COCO results for each interval of the Well #2 compared with the sedimentation rates obtain through manual frequency ratio methodology. The calculation of sedimentation rate through manual frequency ratio method is represented by the black boxes in each interval. The black stars highlight the most probable sedimentation rate obtain with the comparison with both methodologies and the number is in cm/kyr.

Well #3

In Well #3, the MTM of each interval reveals a good correlation between the main GR peak with the lowest frequency and the short eccentricity parameter (97-128 kyr; red stars in *Figure S7*). The second and third peaks, with high power compared to mean value, correlates with the obliquity (41 kyr) and precession parameters (19-23 kyr; respectively orange and blue stars in *Figure S7*). The COCO results further support the manual frequency ratio method (*Figure S8*). The highlight of the short eccentricity cycles allows tuning GR data in depth with a pure 100 kyr periodicity signal to obtain a GR curve in time (blue curve, *Figure S7*).

The new GR curve in time indicate a time span of 4.23 Ma for the Plio-Pleistocene series along the Well #3 (blue curve, *Figure S7*). Finally, after the anchoring on the minima of the long eccentricity cycles, we obtain an age model for the GR data of the Well #3 (orange curve, *Figure S7*). This model generates an age of 4.3 Ma for the arrival of the first terrigenous sediments brought by the Amazon along Well #3 (orange curve, *Figure S7*). The MTM of this curve attributes main cyclicities for 830, 350, 162, 114, 96 and 44 kyr (*Figure S7*). We also calculated sedimentation rates by comparing curves in time and depth; it highlights low sedimentation rates of 39 cm/kyr during I7 (0.8 to 1.2 Ma), and 35, 25 and 38 cm/kyr during I5, I4 and I3 respectively (from 1.6 to 2.8 Ma). Interval I1 (from 3.2 to 4.3 Ma) also reveal low sedimentation rates of 27 cm/kyr (*Figure S7*). Other intervals present high sedimentation rates between present-day to 0.8 Ma (I9 and I8) with value of 52 and 55 cm/kyr respectively as well as interval I6 (1.2 to 1.6 Ma) with a sedimentation rate of 54 cm/kyr and interval I2 (2.8 to 3.2 Ma) with the highest sedimentation rates recorded of 74 cm/kyr (*Figure S7*). Finally, the eCOCO inferred sedimentation rates track those estimated from the 100 kyr tuned GR data (*Figure S9*).

826 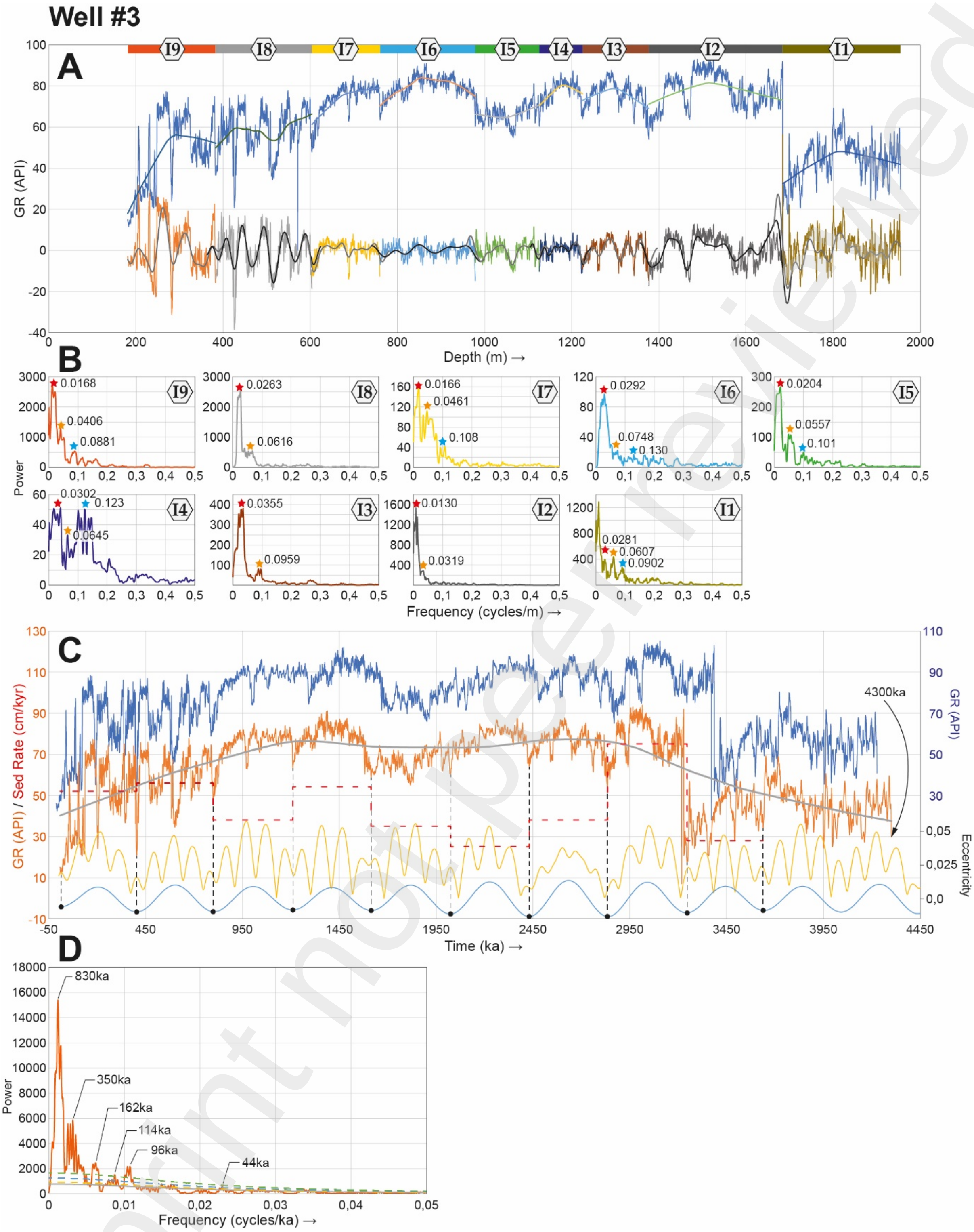

Well #3
A
B
C
D
GR (API)
Depth (m) →
Power
Frequency (cycles/m) →
GR (API) / Sed Rate (cm/kyr)
GR (API)
Eccentricity
4300ka
Time (ka) →
830ka
350ka
162ka
114ka
96ka
44ka
Frequency (cycles/ka) →

Figure S7: Cyclostratigraphic analysis of GR data of Well #3 (depths 181 to 1954 m, Plio-Pleistocene section). (A) Raw and detrended GR data along with the analysed stratigraphic intervals (labelled I1 through I9 from the oldest to the youngest). The filtered wavelength of the short eccentricity is also shown along with the detrended data. (B) 2π-MTM power spectra of the detrended stratigraphic intervals (mentioned by the color codes). Red, orange and blue stars on spectral peaks indicate possible short eccentricity, obliquity and precession related wavelengths. (C) The 100 kyr tuned GR data (blue: tuned to a pure 100 kyr sine curve, orange: the 100 kyr tuned GR curve is anchored to 405 kyr eccentricity cycle minima) along with the raw La2004 eccentricity data (yellow curve) and the filtered 405 kyr cycle band (light blue curve). The red-dashed curve depicts sedimentation rate inferred from the 405 kyr anchored curve. (D) 2π-MTM power spectra of the anchored GR data to 405 kyr cycle minima (in orange), along with the robust red noise levels (median, 90%, 95% and 99% confidence levels).

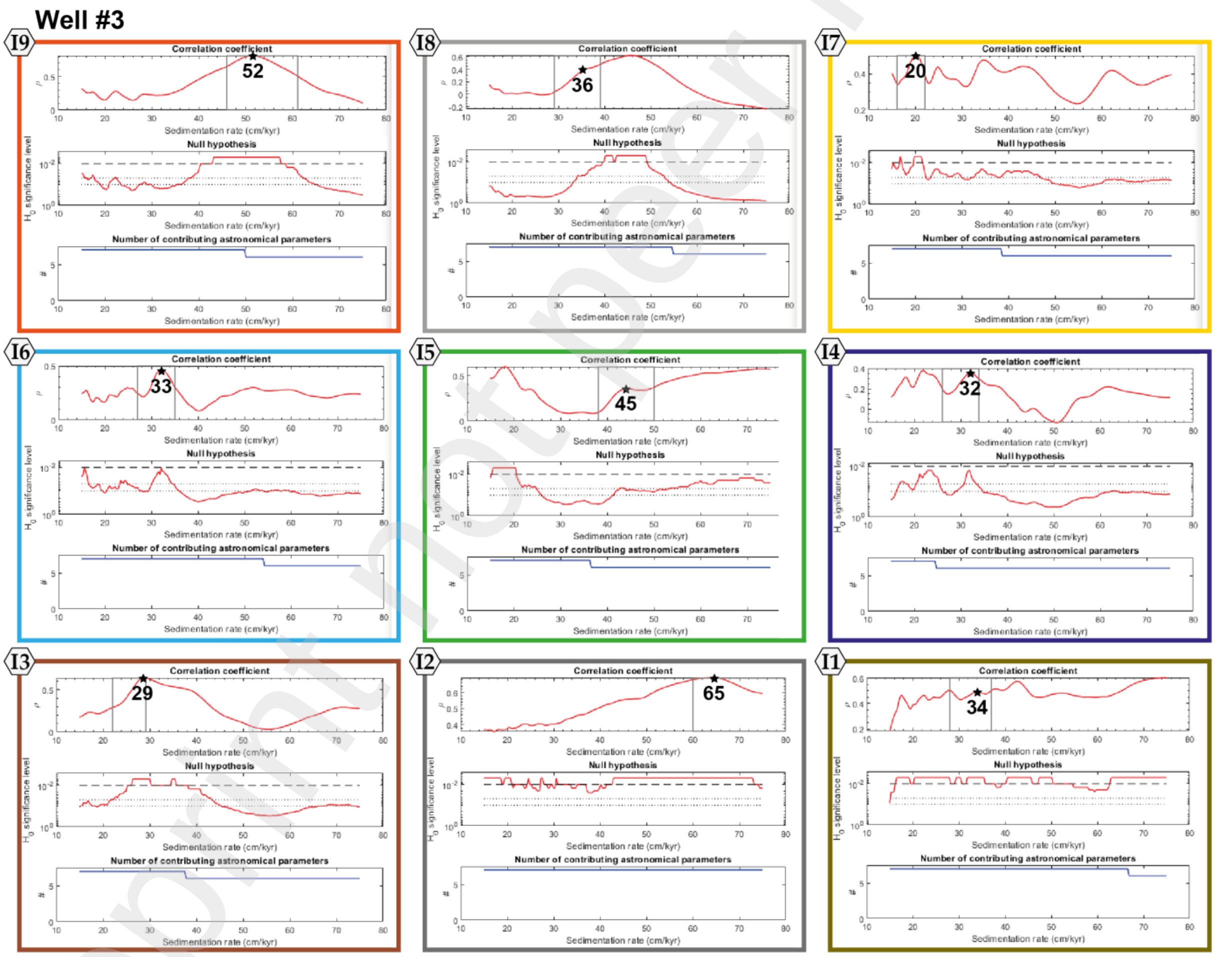

Figure S8: COCO results for each interval of the Well #3 compared with the sedimentation rates obtain through manual frequency ratio methodology. The calculation of sedimentation rate through manual frequency ratio method is represented by the black boxes in each interval. The black stars highlight the *most probable sedimentation rate obtain with the comparison with both methodologies and the number is in cm/kyr.*

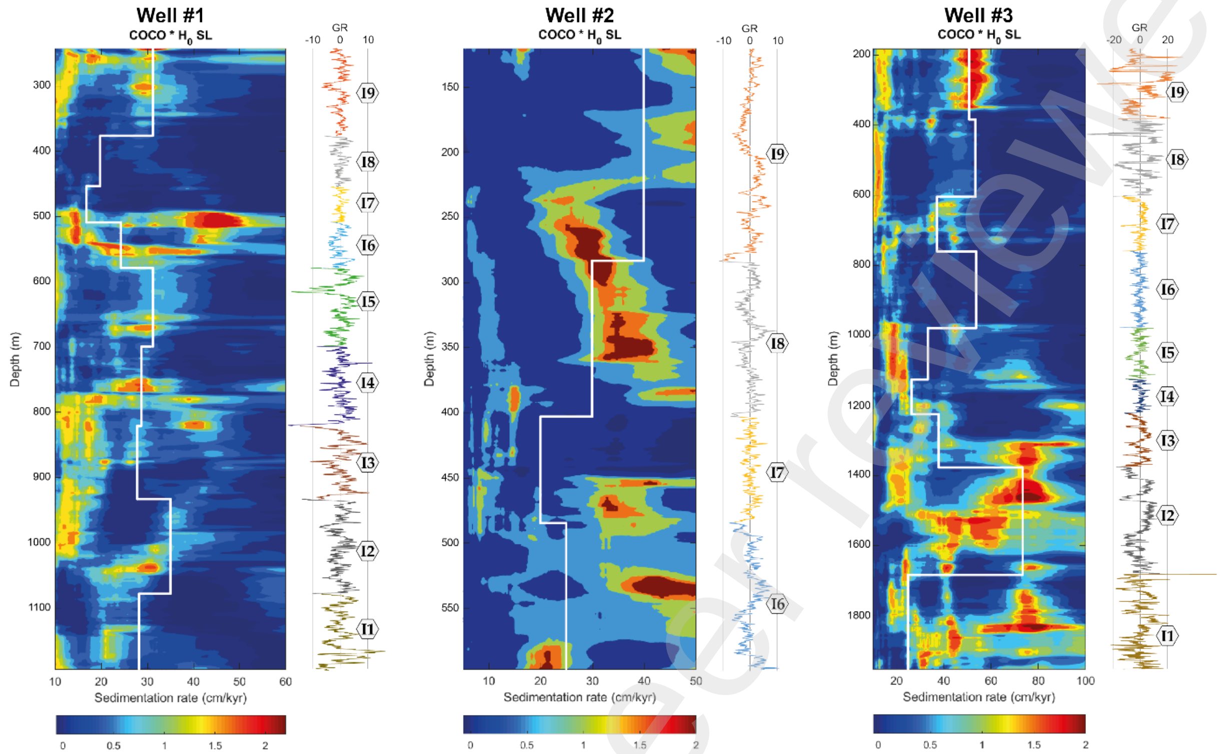

Figure S9: Results of the "eCOCO" method for the three wells along with sedimentation rates inferred from the 100 kyr tuned GR data (stair-like white curves). Pearson correlation coefficient, and Null hypothesis H0 for non-orbital forcing estimated by the evolutive eCOCO approach. Sedimentation rate step is fixed at 0.2 cm/kyr. The used astronomical solution is from Laskar 2004 model (Laskar et al., 2004) with a middle age of the data at 2.0 Ma for wells #1 and #3, and 1.0 Ma for Well #2. The sliding window is fixed at 100, 150 and 200 m for wells #1, #2 and #3 respectively. A step of 1 m is fixed for the three wells.

7.4. Sequence and seismic stratigraphic methods

Catuneanu et al. (2011) redefined a sequence as "a succession of strata deposited during a full cycle of changes in accommodation or sediment supply." In this study, we adopted this definition, using the terms "sequence" or "seismic sequence."

Below, additional information regarding system tracts and their boundaries is presented:

The Transgressive Surface (TS) corresponds to the transition from a coastline shifting toward the basin to a coastline migrating toward the continent. The Maximum Flooding Surface (MFS) represents the top boundary of the Transgressive System Tract (TST) and is characterized by a shift in the migration of the coastline from the coast towards the basin, opposite to the TS.

The Highstand System Tract (HST) is initiated by normal regression when sea-level rise decelerates, and sediment starts to prograde due to a decrease in the A/S ratio. Although the global sea level is still rising, the coastline migrates basinwards due to the dominant role of sediment influx. The upper limit of the HST is defined by the Sequence Boundary (SB). The SB consists of a subaerial erosive surface that develops as sea level falls and the coastline starts to migrate towards the basin, although the foresets of the HST can still remain under submarine conditions.

The Falling Stage System Tract (FSST) wedge shows only a series of downward progradations due to the dominant role of eustatic sea-level fall.

The Lowstand System Tract (LST) continues to develop even after eustatic sea level starts to rise. As long as sediment supplies remain greater than accommodation, the shoreline continues to migrate basinwards. When accommodation overcomes the rate of sediment supply, the shoreline starts to move towards the coastline, which marks the Transgressive Surface.

To distinguish each package, four important factors were considered during seismic facies interpretation (*Figure 3*):

- Morphology of the horizons (erosion, steepness, extent, position)
- Stratal terminations (Onlap, Offlap, Toplap, and Downlap)
- The offlap break position (topset edge), when preserved
- Stacking patterns of successive sedimentary units

7.5. Identification and definition of seismic sequences

Nine seismic sequences were identified through seismic interpretation (S1 to S9, *Figure 4*). Each seismic sequence was interpreted as a full cycle of depositional system tracts by analysing their respective seismic architecture (*Figure 4*). In addition, when the identification of depositional systems tract could also be achieved all together by analyses of wireline log motifs and cyclostratigraphy (*Figures 5 and 6*), we can define with more confidence a sequential stratigraphy for the Pliocene-Pleistocene Amazon shelf. For instance, we can observe an excellent correlation between Transgressive Surface (TS), drops in GR values and lithological transitions from shale to sandstone. It should be noted that TST are not well developed along the area and LST are absent on the shelf. During lowstands, much of the sediments of the

Amazon are probably directly funnelled to the deep-sea fan, therefore, bypassing the outer shelf and are not transported by the longshore current to our study area. This implies that the Sequence Boundary (SB), the Transgressive Surface (TS), and the Maximum Flooding Surface (MFS) are either a common horizon or a small seismic interval in some part of the seismic block.

Sequence S1 displays a thickness of 140 ms TWTT in Well #1 (*Figure 4*). Deposition of S1 starts on top of a high amplitude reflector associated with carbonate lithology. This reflector marks the transition from the Amapá Fm to the Plio-Pleistocene siliciclastic series. On top of this reflector, the first sediments part of the sequence S1 begins to downlap the area, lithological log reveals that these siliciclastic sediments are sandstone (*Figure 2*). Above these sands, the lower part of S1 seismic sequence shows very low amplitude and poorly continuous reflectors with downlapping character, able to build outward and upward into the available space, with very low slope angles. This seismic facies; SF2 (*Figure 3*), is associated with fine-grained sediments on the logs and is interpreted as prodeltaic units of a HST. Two or three reflectors at the end of the HST present toplapping terminations with only progradational behaviour (SF3; *Figure 3*); it seems to be part of a distal FSST with a very small thickness (30 ms TWTT at its thickest part). Above this depositional system tract, the S1 sequence presents moderate to high amplitude reflectors with a rapid increase of steepness and a better continuity of the reflectors. Its base is erosive (red line inside the S1 on *Figure 4*). This unit is interpreted as a SF3 (*Figure 3*) and thus corresponds to a FSST with a rapid shift of the sedimentation towards the basin. However, this FSST begins at a proximal position compared to the two or three reflectors below showing similar seismic facies. It is possible to separate, therefore, this Sequence S1 in two different seismic sequences, yet we interpret the small interval as a sub-sequence related to a smaller scale cyclicity.

Sequence S2 displays a thickness of 120 ms TWTT in Well #1 (*Figure 4*). S2 consists mainly of a thick aggradational sedimentary interval, which downlap the top of the S1 FSST. Low to medium amplitude reflectors are observed in Sequence S2, and are interpreted as a SF2 (*Figure 3*), which corresponds to a HST composed of shales (*Figure 2*). On top of this HST, clinoforms associated with SF3 (*Figure 3*) with only progradational behaviour reveal the presence of a FSST (*Figure 4*). Compared to the FSST of sequence S1, this FSST begins at a distal position and the offlap break position (blue circle in *Figure 4*) is closer to the slope.

Sequence S3 displays a thickness of 100 ms TWTT in Well #1 (*Figure 4*). Contrary to the previous sequence, a high amplitude reflector covers the previous S2 FSST. This reflector is associated with SF1 (*Figure 3*) and represents a small transgressive interval. Prograding and aggrading reflectors associated with HST (SF2; *Figure 3*), overlay the transgressive interval. Clinoforms with only progradational behaviour begins to cover the HST (SF3; *Figure 3*). Compared to the same transition inside sequence S2, the transition from HST to FSST occurs at a proximal point, the offlap break position shows the same proximal migration (*Figure 4*). Foresets of the FSST present elongated shapes that extend towards the shelf and reach the slope (*Figure 4*).

Sequence S4 displays a thickness of 100 ms TWTT in Well #1 (*Figure 4*). At first sight, S4 is mostly composed of stacked sub-parallels reflectors (SF1; *Figure 3*) reaching a thickness of 75 ms TWTT in Well #1 (*Figure 4*). On top of this TST, an interval presents progradational clinoforms (SF4; *Figure 3*) and is associated with a small FSST (30 ms TWTT thick at its thickest part along the Inline 1, FSST inside S1, S2 and S3 reach thickness of 50 to 100 ms TWTT). However, at a finer scale, S4 is composed at its base by three stacked reflectors of high amplitude, which covers the FSST inside sequence S3. This set of sub-parallels reflectors correspond to a thick transgressive interval (SF1; *Figure 3*). Above, on the proximal part of the inline 1 (*Figure 4*), packages of aggrading and oblique reflectors compose a small HST (SF2; *Figure 3*). However, the HST is highly eroded (see orange line corresponding to a Transgressive Surface, inside S4 in the *Figure 4*), the erosive boundary cut through almost the entirety of the HST leaving a gap of 70 ms TWTT of sediments on the most distal part of the outer shelf. The Transgressive Surface (TS), which corresponds to the erosional unconformity, reveals two different reflector amplitude domains. Indeed, the proximal part displays a flat reflector of high amplitude, while the distal part exhibits a highly eroded unconformity with low amplitude reflection. The gap created by this erosion is filled by reflectors of low to medium amplitude with onlap termination toward the coast with sub-parallel and continuous nature (SF1; *Figure 3*). S4 could be separated, therefore, in two different seismic sequences but we decided due to its size to interpret the small HST package in the proximal part of the seismic block as a sub-sequence associated with a smaller scale cyclicity.

Sequence S5 displays thickness of 170 ms TWTT in Well #1 (*Figure 4*). S5 starts with three reflectors corresponding to a SF1 (*Figure 3*) and are characteristics of a TST. The following reflectors show low amplitude associated with intense progradation and low aggradation (SF2; *Figure 3*). The angle of foresets is particularly high (compared to the same feature in the older sequences) while the bottomsets extension is limited (*Figure 4*). It is difficult to identify the point at which aggradation ceases, and the system tract gradually evolve from a HST to a FSST. Finally, FSST progrades through high angle clinoforms along the outer shelf (SF3'; *Figure 3*). The thickness of the FSST is more constant along the outer shelf in this sequence compared to the FSST inside S1, S2 and S3. Closer to the slope, a scar from a submarine landslide affects the foresets of FSST clinoforms but is also buried under the foresets of newly generated clinoforms part of the same FSST inside S5. On the slope, chaotic reflectors (SF5, see *Figure 3*) are visible and correspond to displaced sediments remaining at the foot of the landslide scar. These chaotic reflectors are covered by clinoforms of very low amplitude with mostly prograding nature. However, the aggrading nature of some reflectors could indicate that these clinoforms are part of a LST (SF4; *Figure 3*), which is younger than the Submarine Landslide 1 (SL1, *Figure 4*).

Sequence S6 displays thickness of 90 ms TWTT in Well #1 (*Figure 4*). Transition between Sequence S5 and S6 reveals a highly erosive unconformity that is topped on the slope by sub-parallels reflectors of medium to high amplitude, which correspond to a TST (SF1; *Figure 3*) (*Figure 4*). This TST is the thickest transgressive package observed in the seismic block during the deposition of the Plio-Pleistocene series. It reaches a thickness of more than 100 ms TWTT along the Inline A at its thickest area. The TST is also at a very distal part of the seismic block, which implies a prior important relative sea-level fall. Along the Inline B (*Figure 4*), multiple landslides and deformation affect the slope domain, and therefore the TST reflectors. Above this system tract, reflectors of medium amplitude downlap the previous reflectors and prograde towards the basin with an important aggradational behaviour (SF2; *Figure 3*). Finally, aggradation cease and only prograding reflectors are visible near the slope (*Figure 4*). Along the inline B (*Figure 4*), the erosive unconformity delimiting the S6 and S7 has eroded the most distal part of the regressive cortege, so, the S6 FSST is not visible.

Sequence S7 displays a thickness of 120 ms TWTT in Well #1 (*Figure 4*). The first reflectors associated with S7 are based on an erosive unconformity (Orange line at the interface of S6 and S7 in *Figure 4*). A set of reflectors of high amplitude, associated with SF1, covers this unconformity, and are, therefore, part of a TST. Above the TST, clinoforms prograde towards the basin, most of the clinoforms are only prograding and are related to SF3 (*Figure 3*) and are part of a FSST. Only bottomsets of the previous HST appear inside the seismic block possibly due to its position closer to the continent. Close to the slope, a Submarine Landslide scar cut the end of the FSST. This second Submarine Landslide (SL2) shows the same pattern as the one observed in SL1. Stacked reflectors of low amplitude also cover it, which could be associated with a LST. However, the lack of data towards the basin prevents a clear identification.

Sequence S8 displays a thickness of 70 ms TWTT in Well #1 (*Figure 4*). Along the slope, the thickness of S8 increases drastically. Along the Inline A (*Figure 4*), only clinoforms with extended bottomsets cover the slope. The Inline B (*Figure 4*), reveals more precise patterns, five intervals with clear progradation topped by a high amplitude reflector are identified as SF4 (*Figure 3*) and correspond to FSST/LST (FR 1 to FR 5 in the *Figure 4*) developed on the slope. These regressive systems are at a smaller scale compared to the FSST observed during the previous seismic sequence; indeed, FSST/LST only extend along the slope on stretch of one or two kilometres in width, whereas the previous FSST can extend along the entire width of the all the outer shelf for five to ten kilometres. On the outer shelf, data quality declines and most of the reflectors have poor continuity. However, some area along Inline A reveal a clear stacking of high amplitude reflectors along a stretch as wide as one kilometre. It is associated with SF7 (*Figure 3*) and are related to carbonate build-up.

Sequence S9 displays a thickness of 180 ms TWTT in Well #1 (*Figure 4*). On the outer shelf along the Inline A (*Figure 4*), reflectors of high amplitude highlight topographic features which are associated with SF7 (*Figure 3*) and are characteristic of carbonated build-ups during TST. Poor data quality prevents more detailed interpretation of this area. However, along slope in the Inline B, four intervals: FR 6 to FR 9 (*Figure 4*) which show aggradation and progradation, are topped by high amplitude reflector and correspond to SF4 (*Figure 3*). These intervals correspond to FSST and LST of smaller scale compared to the ones observed in the Sequences S1 to S7. Finally, the sea floor reveals topographic highs along the outer shelf which could be associated with SF7 (*Figure 3*).

References:

Anderson, J.B., Fillon, R.H. (Eds.), 2004. Late Quaternary Stratigraphic Evolution of the Northern Gulf of Mexico Margin. SEPM (Society for Sedimentary Geology). https://doi.org/10.2110/pec.04.79

Barth, A.M., Clark, P.U., Bill, N.S., He, F., Pisias, N.G., 2018. Climate evolution across the Mid-Brunhes Transition. Clim. Past 14, 2071–2087. https://doi.org/10.5194/cp-14-2071-2018

Bartoli, G., Sarnthein, M., Weinelt, M., Erlenkeuser, H., Garbe-Schönberg, D., Lea, D.W., 2005. Final closure of Panama and the onset of northern hemisphere glaciation. Earth Planet. Sci. Lett. 237, 33–44. https://doi.org/10.1016/j.epsl.2005.06.020

Behling, H., W. Arz, H., Pätzold, J., Wefer, G., 2000. Late Quaternary vegetational and climate dynamics in northeastern Brazil, inferences from marine core GeoB 3104-1. Quat. Sci. Rev. 19, 981–994. https://doi.org/10.1016/S0277-3791(99)00046-3

Berger, A., Loutre, M.F., 1994. Precession, Eccentricity, Obliquity, Insolation and Paleoclimates, in: Duplessy, J.-C., Spyridakis, M.-T. (Eds.), Long-Term Climatic Variations. Springer Berlin Heidelberg, Berlin, Heidelberg, pp. 107–151. https://doi.org/10.1007/978-3-642-79066-9_5

Bott, M.H.P., 1992. Passive margins and their subsidence. J. Geol. Soc. 149, 805–812. https://doi.org/10.1144/gsjgs.149.5.0805

Brandao, J.A.S.L., Feijo, F.J., 1994. Amazon river mouth Basin; Bacia da foz do Amazonas. Bol. Geocienc. Petrobras 8.

Campbell, K.E., 2010. Late Miocene onset of the Amazon River and the Amazon deep-sea fan: Evidence from the Foz do Amazonas Basin: COMMENT. Geology 38, 212–212. https://doi.org/10.1130/G30633C.1

Carozzi, A.V., 1981. Porosity models and oil exploration of Amapa Carbonates, Paleogene, Foz Do Amazonas Basin, offshore NW Brazil. J. Pet. Geol. 4, 3–34. https://doi.org/10.1111/j.1747-5457.1981.tb00521.x

Catuneanu, O., 2019. Scale in sequence stratigraphy. Mar. Pet. Geol. 106, 128–159. https://doi.org/10.1016/j.marpetgeo.2019.04.026

Catuneanu, O., 2006. Principles of Sequence Stratigraphy, Elsevier. ed.

Catuneanu, O., Abreu, V., Bhattacharya, J.P., Blum, M.D., Dalrymple, R.W., Eriksson, P.G., Fielding, C.R., Fisher, W.L., Galloway, W.E., Gibling, M.R., Giles, K.A., Holbrook, J.M., Jordan, R., Kendall, C.G.St.C., Macurda, B., Martinsen, O.J., Miall, A.D., Neal, J.E., Nummedal, D., Pomar, L., Posamentier, H.W., Pratt, B.R., Sarg, J.F., Shanley, K.W., Steel, R.J., Strasser, A., Tucker, M.E., Winker, C., 2009. Towards the standardization of sequence stratigraphy. Earth-Sci. Rev. 92, 1–33. https://doi.org/10.1016/j.earscirev.2008.10.003

Catuneanu, O., Galloway, W.E., Kendall, C.G.S. t. C., Miall, A.D., Posamentier, H.W., Strasser, A., Tucker, M.E., 2011. Sequence Stratigraphy: Methodology and Nomenclature. Newsl. Stratigr. 44, 173–245. https://doi.org/10.1127/0078-0421/2011/0011

Chalk, T.B., Hain, M.P., Foster, G.L., Rohling, E.J., Sexton, P.F., Badger, M.P.S., Cherry, S.G., Hasenfratz, A.P., Haug, G.H., Jaccard, S.L., Martínez-García, A., Pälike, H., Pancost, R.D., Wilson, P.A., 2017. Causes of ice age intensification across the Mid-Pleistocene Transition. Proc. Natl. Acad. Sci. 114, 13114–13119. https://doi.org/10.1073/pnas.1702143114

Chima, K.I., Gorini, C., Rabineau, M., Granjeon, D., Do Couto, D., Leroux, E., Hoggmascall, N., 2020. Pliocene and Pleistocene stratigraphic evolution of the western Niger Delta intraslope basins: A record of glacio-eustatic sea-level and basin tectonic forcings. Glob. Planet. Change 195, 103355. https://doi.org/10.1016/j.gloplacha.2020.103355

Clark, P.U., Archer, D., Pollard, D., Blum, J.D., Rial, J.A., Brovkin, V., Mix, A.C., Pisias, N.G., Roy, M., 2006. The middle Pleistocene transition: characteristics, mechanisms, and implications for long-term changes in atmospheric pCO2. Quat. Sci. Rev. 25, 3150–3184. https://doi.org/10.1016/j.quascirev.2006.07.008

Cleveland, W.S., 1979. Robust locally weighted regression and smoothing scatterplots. J. Am. Stat. Assoc. 74, 829–836.

Crivellari, S., Chiessi, C.M., Kuhnert, H., Häggi, C., da Costa Portilho-Ramos, R., Zeng, J.-Y., Zhang, Y., Schefuß, E., Mollenhauer, G., Hefter, J., Alexandre, F., Sampaio, G., Mulitza, S., 2018. Increased Amazon freshwater discharge during late Heinrich Stadial 1. Quat. Sci. Rev. 181, 144–155. https://doi.org/10.1016/j.quascirev.2017.12.005

Cruz, A.M., 2018. Integrated geological and geophysical studies applied to understanding the evolution of the Offshore Amazon Basin. Sorbonne Université.

Cruz, A.M., Reis, A.T., Suc, J.P., Silva, C.G., Praeg, D., Granjeon, D., Rabineau, M., Popescu, S.M., Gorini, C., 2019. Neogene evolution and demise of the Amapá carbonate platform, Amazon continental margin, Brazil. Mar. Pet. Geol. 105, 185–203. https://doi.org/10.1016/j.marpetgeo.2019.04.009

Dai, A., Trenberth, K.E., 2002. Estimates of Freshwater Discharge from Continents: Latitudinal and Seasonal Variations. J. Hydrometeorol. 3, 660–687. https://doi.org/10.1175/1525-7541(2002)003<0660:EOFDFC>2.0.CO;2

Damuth, J.E., Kowsmann, R.O., Flood, R.D., Belderson, R.H., Gorini, M.A., 1983. Age relationships of distributary channels on Amazon deep-sea fan: Implications for fan growth pattern. Geology 11, 470. https://doi.org/10.1130/0091-7613(1983)11<470:ARODCO>2.0.CO;2

Damuth, J.E., Kumar, N., 1975. Amazon Cone: Morphology, Sediments, Age, and Growth Pattern. Geol. Soc. Am. Bull. 86, 863. https://doi.org/10.1130/0016-7606(1975)86<863:ACMSAA>2.0.CO;2

Darros de Matos, R.M., 2000. Tectonic evolution of the equatorial South Atlantic, in: Mohriak, W., Taiwani, M. (Eds.), Geophysical Monograph Series. American Geophysical Union, Washington, D. C., pp. 331–354. https://doi.org/10.1029/GM115p0331

De Schepper, S., Groeneveld, J., Naafs, B.D.A., Van Renterghem, C., Hennissen, J., Head, M.J., Louwye, S., Fabian, K., 2013. Northern Hemisphere Glaciation during the Globally Warm Early Late Pliocene. PLoS ONE 8, e81508. https://doi.org/10.1371/journal.pone.0081508

Dowsett, H.J., Caballero Gill, R.P., 2010. Pliocene Climate. Stratigraphy 7.

Driscoll, Neal W., Karner, G.D., 1994. Flexural deformation due to Amazon Fan loading: A feedback mechanism affecting sediment delivery to margins. Geology 1015–1018.

Droxler, A.W., Jorry, S.J., 2021. The Origin of Modern Atolls: Challenging Darwin’s Deeply Ingrained Theory. Annu. Rev. Mar. Sci. 39.

Eisma, D., van der Marel, H.W., 1971. Marine muds along the Guyana coast and their origin from the Amazon basin. Contrib. Mineral. Petrol. 31, 321–334. https://doi.org/10.1007/BF00371152

Figueiredo, J. de J.P., Zalàn, P.V., Soares, E.F., 2007. Bacia da foz do Amazonas. Bol. Geociências Petrobrás 299–309.

Figueiredo, J., Hoorn, C., van der Ven, P., Soares, E., 2010. Late Miocene onset of the Amazon River and the Amazon deep-sea fan: Evidence from the Foz do Amazonas Basin: Reply. Geology 38, e213–e213. https://doi.org/10.1130/G31057Y.1

Figueiredo, J., Hoorn, C., van der Ven, P., Soares, E., 2009. Late Miocene onset of the Amazon River and the Amazon deep-sea fan: Evidence from the Foz do Amazonas Basin. Geology 37, 619–622. https://doi.org/10.1130/G25567A.1

Flood, R.D., Piper, D.J.W., Shipboard Scientific Party, 1995. PODPIR (Proceedings of the Ocean Drilling Program, Initial Reports No. 155).

Gensac, E., Martinez, J.-M., Vantrepotte, V., Anthony, E.J., 2016. Seasonal and inter-annual dynamics of suspended sediment at the mouth of the Amazon river: The role of continental and oceanic forcing, and implications for coastal geomorphology and mud bank formation. Cont. Shelf Res. 118, 49–62. https://doi.org/10.1016/j.csr.2016.02.009

Giachini Tosetto, E., Bertrand, A., Neumann-Leitão, S., Nogueira Júnior, M., 2022. The Amazon River plume, a barrier to animal dispersal in the Western Tropical Atlantic. Sci. Rep. 12, 537. https://doi.org/10.1038/s41598-021-04165-z

Gorini, C., Haq, B.U., dos Reis, A.T., Silva, C.G., Cruz, A., Soares, E., Grangeon, D., 2014. Late Neogene sequence stratigraphic evolution of the *Foz do Amazonas* Basin, Brazil. Terra Nova 26, 179–185. https://doi.org/10.1111/ter.12083

Harris, S.E., Mix, A.C., 1999. Pleistocene Precipitation Balance in the Amazon Basin Recorded in Deep Sea Sediments. Quat. Res. 51, 14–26. https://doi.org/10.1006/qres.1998.2008

Haywood, A.M., Dowsett, H.J., Valdes, P.J., Lunt, D.J., Francis, J.E., Sellwood, B.W., 2009. Introduction. Pliocene climate, processes and problems. Philos. Trans. R. Soc. Math. Phys. Eng. Sci. 367, 3–17. https://doi.org/10.1098/rsta.2008.0205

Helland-Hansen, W., Gjelberg, J.G., 1994. Conceptual basis and variability in sequence stratigraphy: a different perspective. Sediment. Geol. 92, 31–52.

Hoorn, C., 1997. Palynology of the Pleistocene glacial/interglacial cycles of the Amazon Fan (Holes 940A, 944A, and 946A)., in: Flood, R.D., Piper, D.J.W., Klaus, A., Peterson, L.C. (Eds.), Proceedings of the Ocean Drilling Program, 155 Scientific Results, Proceedings of the Ocean Drilling Program. Ocean Drilling Program, pp. 397–410. https://doi.org/10.2973/odp.proc.sr.155.1997

Hoorn, C., Bogotá-A, G.R., Romero-Baez, M., Lammertsma, E.I., Flantua, S.G.A., Dantas, E.L., Dino, R., do Carmo, D.A., Chemale, F., 2017. The Amazon at sea: Onset and stages of the Amazon River from a marine record, with special reference to Neogene plant turnover in the drainage basin. Glob. Planet. Change 153, 51–65. https://doi.org/10.1016/j.gloplacha.2017.02.005

Hu, C., Montgomery, E., Schmitt, R., Mullerkarger, F., 2004. The dispersal of the Amazon and Orinoco River water in the tropical Atlantic and Caribbean Sea: Observation from space and S-PALACE floats. Deep Sea Res. Part II Top. Stud. Oceanogr. 51, 1151–1171. https://doi.org/10.1016/S0967-0645(04)00105-5

Hunt, D., Tucker, M.E., 1992. Stranded parasequences and the forced regressive wedge systems tract: deposition during base-level'fall. Sediment. Geol. 81, 1–9. https://doi.org/10.1016/0037-0738(92)90052-S

Jacobs, M.B., Ewing, M., 1969. Suspended particulate matter: concentration in the major oceans. Science 163, 380–383.

Jouzel, J., Masson-Delmotte, V., Cattani, O., Dreyfus, G., Falourd, S., Hoffmann, G., Minster, B., Nouet, J., Barnola, J.M., Chappellaz, J., Fischer, H., Gallet, J.C., Johnsen, S., Leuenberger, M., Loulergue, L., Luethi, D., Oerter, H., Parrenin, F., Raisbeck, G., Raynaud, D., Schilt, A., Schwander, J., Selmo, E., Souchez, R., Spahni, R., Stauffer, B., Steffensen, J.P., Stenni, B., Stocker, T.F., Tison, J.L., Werner, M., Wolff, E.W., 2007. Orbital and Millennial Antarctic Climate Variability over the Past 800,000 Years. Science 317, 793–796. https://doi.org/10.1126/science.1141038

Kleiven, H.F., Jansen, E., Fronval, T., Smith, T.M., 2002. Intensification of Northern Hemisphere glaciations in the circum Atlantic region (3.5–2.4 Ma)–ice-rafted detritus evidence.

Lafosse, M., Gorini, C., Le Roy, P., Alonso, B., d'Acremont, E., Ercilla, G., Rabineau, M., Vázquez, J.T., Rabaute, A., Ammar, A., 2018. Late Pleistocene-Holocene history of a tectonically active segment of the continental margin (Nekor basin, Western Mediterranean, Morocco). Mar. Pet. Geol. 97, 370–389. https://doi.org/10.1016/j.marpetgeo.2018.07.022

Laskar, J., Robutel, P., Joutel, F., Gastineau, M., Correia, A.C.M., Levrard, B., 2004. A long-term numerical solution for the insolation quantities of the Earth. Astron. Astrophys. 428, 261–285. https://doi.org/10.1051/0004-6361:20041335

Li, M., Hinnov, L., Kump, L., 2019. Acycle: Time-series analysis software for paleoclimate research and education. Comput. Geosci. 127, 12–22. https://doi.org/10.1016/j.cageo.2019.02.011

Lisiecki, L.E., Raymo, M.E., 2005. A Pliocene-Pleistocene stack of 57 globally distributed benthic $\delta^{18}O$ records. Paleoceanography 20. https://doi.org/10.1029/2004PA001071

Lobo, F.J., Ridente, D., 2014. Stratigraphic architecture and spatio-temporal variability of high-frequency (Milankovitch) depositional cycles on modern continental margins: An overview. Mar. Geol. 352, 215–247. https://doi.org/10.1016/j.margeo.2013.10.009

Malhi, Y., Roberts, J.T., Betts, R.A., Killeen, T.J., Li, W., Nobre, C.A., 2008. Climate Change, Deforestation, and the Fate of the Amazon. Science 319, 169–172. https://doi.org/10.1126/science.1146961

Maslin, M., Knutz, P.C., Ramsay, T., 2006. Millennial-scale sea-level control on avulsion events on the Amazon Fan. Quat. Sci. Rev. 25, 3338–3345. https://doi.org/10.1016/j.quascirev.2006.10.012

Maslin, M.A., Li, X.S., Loutre, M.-F., Berger, A., 1998. The contribution of orbital forcing to the progressive intensification of Northern Hemisphere glaciation. Quat. Sci. Rev. 17, 411–426. https://doi.org/10.1016/S0277-3791(97)00047-4

Mason, C.C., Romans, B.W., Stockli, D.F., Mapes, R.W., Fildani, A., 2019. Detrital zircons reveal sea-level and hydroclimate controls on Amazon River to deep-sea fan sediment transfer. Geology 47, 563–567. https://doi.org/10.1130/G45852.1

Merkel, R.H., 1979. Geologic Analysis, in: Well Log Formation Evaluation.

Meyers, S.R., Sageman, B.B., 2007. Quantification of deep-time orbital forcing by average spectral misfit. Am. J. Sci. 307, 773–792. https://doi.org/10.2475/05.2007.01

Miller, K.G., Browning, J.V., Schmelz, W.J., Kopp, R.E., Montain, G.S., Wright, J.D., 2020. Cenozoic sea-level and cryospheric evolution from deep-sea geochemical and continental margin records. Sci. Adv. 6.

Milliman, J.D., 2001. River inputs. Encycl. Ocean Sci. https://doi.org/doi:10.1006/rwos.2001.0074.

Milliman, J.D., Summerhayes, C.P., Barretto, H.T., 1975. Quaternary Sedimentation on the Amazon Continental Margin: A Model. Geol. Soc. Am. Bull. 86, 610. https://doi.org/10.1130/0016-7606(1975)86<610:QSOTAC>2.0.CO;2

Mitsui, T., Boers, N., 2022. Machine learning approach reveals strong link between obliquity amplitude increase and the Mid-Brunhes transition. Quat. Sci. Rev. 277, 107344. https://doi.org/10.1016/j.quascirev.2021.107344

Nace, T.E., Baker, P.A., Dwyer, G.S., Silva, C.G., Rigsby, C.A., Burns, S.J., Giosan, L., Otto-Bliesner, B., Liu, Z., Zhu, J., 2014. The role of North Brazil Current transport in the paleoclimate of the Brazilian Nordeste margin and paleoceanography of the western tropical Atlantic during the late Quaternary. Palaeogeogr. Palaeoclimatol. Palaeoecol. 415, 3–13. https://doi.org/10.1016/j.palaeo.2014.05.030

Nittrouer, C.A., Kuehl, S.A., Demaster, D.J., Kowsmann, R.O., 1986. The deltaic nature of Amazon shelf sedimentation. Geol. Soc. Am. Bull. 97, 444. https://doi.org/10.1130/0016-7606(1986)97<444:TDNOAS>2.0.CO;2

Paillard, D., Labeyrie, L., Yiou, P., 1996. Macintosh Program performs time-series analysis. Eos Trans. Am. Geophys. Union 77, 379–379. https://doi.org/10.1029/96EO00259

Pisias, N.G., Moore, T.C., 1981. The evolution of Pleistocene climate: A time series approach. Earth Planet. Sci. Lett. 52, 450–458. https://doi.org/10.1016/0012-821X(81)90197-7

Rabineau, M., Berné, S., Aslanian, D., Olivet, J.-L., Joseph, P., Guillocheau, F., Bourillet, J.-F., Ledrezen, E., Granjeon, D., 2005. Sedimentary sequences in the Gulf of Lion: A record of 100,000 years climatic cycles. Mar. Pet. Geol. 22, 775–804. https://doi.org/10.1016/j.marpetgeo.2005.03.010

Rabineau, M., Berné, S., Olivet, J.-L., Aslanian, D., Guillocheau, F., Joseph, P., 2006. Paleo sea levels reconsidered from direct observation of paleoshoreline position during Glacial Maxima (for the last 500,000 yr). Earth Planet. Sci. Lett. 252, 119–137. https://doi.org/10.1016/j.epsl.2006.09.033

Rabineau, M., Leroux, E., Aslanian, D., Bache, F., Gorini, C., Moulin, M., Molliex, S., Droz, L., Dos Reis, A.T., Rubino, J.L., Guillocheau, F., Olivet, J.L., 2014. Quantifying subsidence and isostatic readjustment using sedimentary paleomarkers, example from the Gulf of Lion. Earth Planet. Sci. Lett. 388, 353–366. https://doi.org/10.1016/j.epsl.2013.11.059

Raymo, M.E., Oppo, D.W., Curry, W., 1997. The Mid-Pleistocene climate transition: A deep sea carbon isotopic perspective. Paleoceanography 12, 546–559. https://doi.org/10.1029/97PA01019

Ridente, D., Trincardi, F., Piva, A., Asioli, A., 2009. The combined effect of sea level and supply during Milankovitch cyclicity: Evidence from shallow-marine δ18O records and sequence architecture (Adriatic margin). Geology 37, 1003–1006. https://doi.org/10.1130/G25730A.1

Rodger, M., Watts, A.B., Greenroyd, C.J., Peirce, C., Hobbs, R.W., 2006. Evidence for unusually thin oceanic crust and strong mantle beneath the Amazon Fan. Geology 34, 1081. https://doi.org/10.1130/G22966A.1

Ruffell, A.H., Worden, R.H., 1999. Palaeoclimate Controls on Spectral Gamma-Ray Radiation from Sandstones, in: Worden, Richard H., Morad, S. (Eds.), Clay Mineral Cements in Sandstones. Blackwell Publishing Ltd., Oxford, UK, pp. 93–108. https://doi.org/10.1002/9781444304336.ch4

Ruffell, A.H., Worden, R.H., Evans, R., 1999. Paleoclimate Controls on Spectral Gamma-Ray Radiation from Sandstones. Clay Miner. Cem. Sandstones 93–108.

Rühlemann, C., Diekmann, B., Mulitza, S., Frank, M., 2001. Late Quaternary changes of western equatorial Atlantic surface circulation and Amazon lowland climate recorded in Ceará Rise deep-sea sediments. Paleoceanography 16, 293–305. https://doi.org/10.1029/1999PA000474

Silva, S.R.P., Maciel, R.R., Severino, M.C.G., 1998. Cenozoic tectonics of Amazon Mouth Basin. Geo-Mar. Lett. 18, 256–262. https://doi.org/10.1007/s003670050077

Thomson, D.J., 1982. Spectrum estimation and harmonic analysis. Proc. IEEE 70, 1055–1096. https://doi.org/10.1109/PROC.1982.12433

Vale, N.F., Braga, J.C., De Moura, R.L., Salgado, L.T., De Moraes, F.C., Karez, C.S., De Carvalho, R.T., Salomon, P.S., Menandro, P.S., Amado-Filho, G.M., Bastos, A.C., 2022. Distribution, morphology and composition of mesophotic 'reefs' on the Amazon Continental Margin. Mar. Geol. 447, 106779. https://doi.org/10.1016/j.margeo.2022.106779

Weedon, G.P., Coe, A.L., Gallois, R.W., 2004. Cyclostratigraphy, orbital tuning and inferred productivity for the type Kimmeridge Clay (Late Jurassic), Southern England. J. Geol. Soc. 161, 655–666. https://doi.org/10.1144/0016-764903-073

Willeit, M., Ganopolski, A., Calov, R., Brovkin, V., 2019. Mid-Pleistocene transition in glacial cycles explained by declining CO2 and regolith removal. Sci. Adv. 5, eaav7337.

Wohlfarth, B., Björck, S., Funder, S., Houmark-Nielsen, M., Ingólfsson, O., Lunkka, J.P., Vorren, T., 2008. Quaternary of Norden. Episodes J. Int. Geosci. 31, 73–81.

Wolff, B., Carozzi, A.V., 1984. Microfacies, depositional environments, and diagenesis of the Amapá carbonates (Paleocene–middle Miocene), University of Illinois at Urbana-Champaign. ed. Foz do Amazonas Basin, offshore NE Brazil.

Wu, H., Zhang, S., Jiang, G., Hinnov, L., Yang, T., Li, H., Wan, X., Wang, C., 2013. Astrochronology of the Early Turonian–Early Campanian terrestrial succession in the Songliao Basin, northeastern China and its implication for long-period behavior of the Solar System. Palaeogeogr. Palaeoclimatol. Palaeoecol. 385, 55–70. https://doi.org/10.1016/j.palaeo.2012.09.004

Zhang, Y., Chiessi, C.M., Mulitza, S., Zabel, M., Trindade, R.I.F., Hollanda, M.H.B.M., Dantas, E.L., Govin, A., Tiedemann, R., Wefer, G., 2015. Origin of increased terrigenous supply to the NE South American continental margin during Heinrich Stadial 1 and the Younger Dryas. Earth Planet. Sci. Lett. 432, 493–500. https://doi.org/10.1016/j.epsl.2015.09.054